nuclear fusion
IAEA

PAPER • OPEN ACCESS

Design scoping and systems modelling of ST-E1 using the PyTok power plant simulation code

To cite this article: C.L. Wilson *et al* 2026 *Nucl. Fusion* **66** 086002

View the article online for updates and enhancements.

You may also like

- Tokamak Energy's pre-concept design for a fusion power plant: an overview of ST-E1
J. Willis, S.A.M. McNamara, E.N.J. Maartensson et al.
- Foreword to the focus collection: pre-conceptual design of ST-E1 - Tokamak Energy's perspective on pilot plants
M. Porton
- Integrated physics and magnet design for the ST-E1 fusion power plant
E.N.J. Maartensson, N. Welch, M. Scarpari et al.

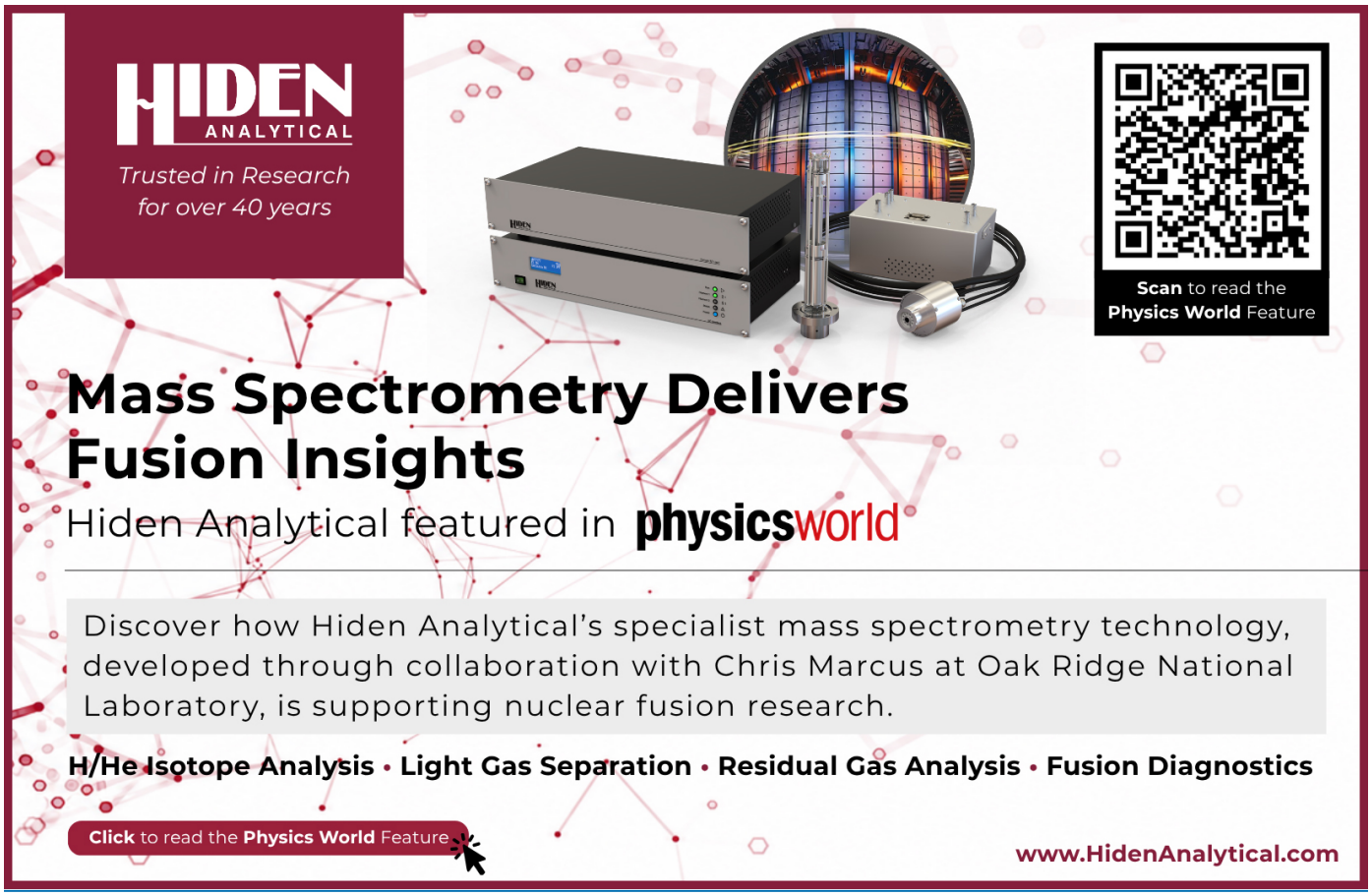

This content was downloaded from IP address 130.51.23.114 on 02/11/2026 at 03:06

OPEN ACCESS
IOP Publishing | International Atomic Energy Agency
Nuclear Fusion
Nucl. Fusion **66** (2026) 086002 (21pp)
https://doi.org/10.1088/1741-4326/ae5d55

Design scoping and systems modelling of ST-E1 using the PyTok power plant simulation code

C.L. Wilson[1], J. Astbury[1], M.J. Ginsberg[2], N. Hinton[1], E.N.J. Maartensson[1], S.A.M. McNamara[1,*], J. Willis[1], E. Yildirim[1] and the ST-E1 Team

[1] Tokamak Energy, Ltd, Oxford, United Kingdom of Great Britain and Northern Ireland
[2] Tokamak Energy, Inc., Washington, DC, United States of America

E-mail: steven.mcnamara@tokamakenergy.com

Received 18 December 2025, revised 19 March 2026
Accepted for publication 9 April 2026
Published 10 July 2026

Abstract

To support the pre-concept design of Tokamak Energy's (TEs) ST-E1 fusion power plant, we developed a new systems code, PyTok. PyTok codifies plasma physics and engineering constraints within a pure Python, object-oriented framework designed for rapid design iteration and exploration of the power-plant parameter space. The code base and its human- and machine-readable data structures enable coupling to external physics codes and data-analysis tools. Informed by TEs design philosophy and techno-economic analyses, the code was used to identify an initial reference design point for ST-E1. A commercially competitive fusion power plant is achievable with a tokamak power core of major radius 5.0 m, aspect ratio $1.9 \leqslant A \leqslant 2.3$ and toroidal field $3.25 \leqslant B_{\mathrm{T}} \leqslant 5.25$ T. The selected design point serves both as a pilot plant and as a commercially competitive reactor using the same permanent power core hardware, enabled by an in-vessel component upgrade phase. The commercial phase targets steady-state operation and a normalised capital expenditure of \$12 000–15 000 per $\mathrm{kW_e}$, corresponding to a fusion power of 2.0–2.5 GW and a net electric power of 800–1000 MW.

Keywords: system modelling, integrated modelling, power plant

(Some figures may appear in colour only in the online journal)

1. Introduction

Under the U.S. Department of Energy's Milestone-Based Fusion Energy Development Program, Tokamak Energy (TE) has produced a pre-concept design of ST-E1, a fusion power plant with a low aspect ratio tokamak power core. Its distinct two-phase mission solves a critical problem of commercial fusion: pilot plants are critical for de-risking physics, engineering, and operational performance, but their high upfront capital requirements and limited lifetime energy production make them challenging to finance. ST-E1 will have three phases of operations: a pilot phase, aiming to de-risk technological and scientific challenges; an upgrade phase to increase fusion power and reduce recirculating power; and finally, a 30 full-power year commercially competitive phase.

In mature thermal power plant technologies, the electrical recirculating power required by the heat island to operate is a small fraction of the overall power produced. Furthermore, the heat island and the power island are largely decoupled. This is not the case for a fusion power plant; a tokamak may require a large fraction of the plant generated electrical power for plasma heating, current drive, magnetic confinement, control systems, and coolant circulation. The circular dependency

* Author to whom any correspondence should be addressed.

Original content from this work may be used under the terms of the Creative Commons Attribution 4.0 licence. Any further distribution of this work must maintain attribution to the author(s) and the title of the work, journal citation and DOI.

 © 2026 The Author(s). Published by IOP Publishing Ltd on behalf of the IAEA

of the power core on the power the plant produces means that the design of a fusion power plant must consider the whole system as an integrated unit from the start. Swanson [1] gives a concise overview of the different types of fusion reactor systems codes that have been described in literature and highlights some of the issues associated with the adoption of existing codes. These tend to encourage proliferation of bespoke tools, making them harder to adapt in new organisations. The TE Systems Code was an explicitly low-fidelity tool primarily aimed at identifying favourable plasma physics operating points for low aspect ratio tokamaks [2], but with few engineering feasibility checks.

To facilitate the pre-concept design of ST-E1, a new systems code, PyTok, was developed that codified TEs plasma and engineering principles, derived from experience of the design, construction and operation of ST40 [3] and several generations of state-of-the-art high-temperature superconducting magnet systems. A modular, extensible framework meant that new models could be easily implemented to better describe different aspects of the physics and engineering and to selectively introduce coupling to higher-fidelity codes. Coleman and McIntosh discuss the limitations of existing fusion reactor systems codes such as PROCESS [4, 5] and SYCOMORE [6] as motivation for the development of BLUEPRINT [7]. These codes produce text output that must be manually processed to produce 2D and 3D models suitable for downstream analysis. PyTok was designed to minimise the issue of speed and consistency that manual processing entails by using in-memory coupling to FreeCAD [8] and direct output of 2D data and plots [9], as well as Sankey diagrams [10] and economic models. However, the scope does not extend to tightly-coupled high-fidelity integrated reactor modelling, such as that exemplified by the FERMI/FREDA codes [11, 12]. Thus, PyTok is closest to BLUEPRINT in functionality but has a narrower scope. Adoption of that code was considered; the main motivation for a bespoke tool was to incorporate TEs technical expertise and to enable rapid adaptation of the code during the power plant design process. PyTok enabled a small integrated design team to rapidly explore a broad parameter space to identify regions that satisfied the objectives of the power plant while respecting constraints; feedback from investigation of these design spaces using higher-fidelity codes was incorporated and PyTok models updated for the next design iteration.

Fusion power plants based on pulsed operation may be strongly limited by cyclic fatigue, resulting in frequent maintenance requirements and reduced availability. For a compact inductively driven reactor, operation with a 1000 s pulse length corresponds to approximately 25 000 pulses per year. Under such conditions, severe cyclic thermal loading of plasma-facing components and blankets is expected, further degrading plant availability. The fatigue lifetime of the central solenoid is typically limited to on the order of 10 000–30 000 cycles [13]. As shown in [14], accommodating a higher number of cycles requires increasing the solenoid outer radius-and consequently the overall machine size-due to the need for additional structural support. Achieving a commercially relevant lifetime of 20–30 years would therefore require a very large central solenoid, either to enable pulse lengths exceeding 8 h or to mitigate cyclic fatigue.

TEs solution to this is a low aspect ratio tokamak power plant with fully non-inductive auxiliary current drive, theoretically enabling steady-state plasmas. While conventional aspect ratio advanced tokamaks can access non-inductive current drive scenarios, a lower self-driven (bootstrap) current fraction may make them less efficient than lower aspect ratio configurations. The principal disadvantage of low aspect ratio tokamaks is the narrow centre column, which constrains the space available for magnet, blanket, vacuum systems, and thermal insulation.

The new systems code, PyTok was used to explore the trade-offs between aspect ratio, toroidal field strength, tritium breeding ratio, and major radius. This was done within the context of commercial viability to determine the range of parameters suitable for a fusion power plant with a low aspect ratio tokamak power core.

Section 2 of this paper provides details of the new systems code framework and the models implemented in the software; section 3 describes the principles behind TEs approach to power plant design, the high-level parameters selected for the plant, and the reference design point for the Pilot phase of plant operation; section 4 discusses the commercial outlook for a family of plants based on the ST-E1 design; and section 5 concludes the paper.

2. PyTok power plant simulation code

2.1. Framework

PyTok originated as a merger of TEs in-house plasma physics systems code and HTS magnet systems code, both of which were developed in Matlab®. It is a pure-Python object-orientated framework, with classes representing the major systems of a tokamak:

- Plasma
- Toroidal field magnets
- Central solenoid
- Poloidal field (equilibrium) Magnets
- Inboard blanket (radiation shield)
- Outboard blanket
- Divertor (including blanket/radiation shield)
- Vacuum chamber
- Primary coolant(s)

Instances of each of these classes are attributes of an overarching Tokamak class, which may itself be an attribute of a Power Plant class. Inputs and outputs are in Javascript Object Notation (JSON) to ensure human and machine readability. The classes are contained in a Python package and dependencies were restricted to those that are available as Python packages through the pip installer to avoid a complex software stack. Using an automated method of operating point selection, described below, and the object-oriented framework it is possible to create simple scripts that iterate an arbitrary number of input parameters. The Python Multiprocessing package

is used to trivially parallelise parameter space exploration and the JSON output formats can be parsed with the Pandas Python package [15, 16] for in-depth data analysis and visualisation. PyTok thus enables all the approaches outlined by Swanson [1] to be followed: explicit modelling of single design points; optimisation; and database generation and filtering.

PyTok develops self-consistent plasma operating points using 0D physics models, ensuring power and current balance and respecting stability limits. Engineering feasibility is determined by a series of models that calculate the current density in the superconducting toroidal field electromagnet winding; the peak field on the superconductor; the quench safety of the winding; the in-plane stress in the winding and case; and the operational life of the winding based on neutron-induced degradation of critical current. The plasma and tokamak engineering are strongly coupled in the code and solutions that satisfy all the constraints are found by iteration. By bringing the major features of a fusion power plant together in a maintainable and extensible framework, consistent designs could be more readily explored and new features added. The remainder of this section describes the models and capabilities that are implemented in the framework.

2.2. Plasma geometry and kinetic profiles

PyTok uses a series of simplified physics models to produce consistent plasma operating points that are in power and current balance. The plasma kinetic profiles are defined using the normalised poloidal flux coordinate, ψ_N and it is assumed that $\psi_N = \rho^2$ [4], where ρ is the normalised minor radius. Profile options include simple parabolic profiles of the form:

$$Y(x) = Y_0 \left(1 - \psi_N\right)^{S_Y} \tag{1}$$

where Y_0 is the on-axis value and S_Y the parabolic shaping exponent. Exponents for temperature and density can be defined independently. Profiles can also be defined using the EPED formulation [17]:

$$\begin{aligned} Y(\psi_N) = y_{\text{sep}} + a_{y0} \Bigg\{ &\tanh\left[\frac{2\left(1-\psi_{N,\text{mid}}\right)}{\Delta}\right] \\ &-\tanh\left[\frac{2\left(\psi_N-\psi_{N,\text{mid}}\right)}{\Delta}\right]\Bigg\} \\ &+ a_{y1}\text{H}\left(1-\frac{\psi_N}{\psi_{N,\text{ped}}}\right)\left[1-\left(\frac{\psi_N}{\psi_{N,\text{ped}}}\right)^{\alpha_{y1}}\right]^{\alpha_{y2}} \end{aligned} \tag{2}$$

where the quantity y is either the electron temperature or density, Δ is the pedestal width in ψ_N space and H is the Heaviside step function.

The flux surface and last closed flux surface geometry is defined using one of three parametrisations: Miller *et al* [18], Ludwig *et al* [19] and a Fourier-like parametrisation. By default the Miller parametrisation is used, which has the form:

$$\begin{aligned} R(r,\theta) = R_{\text{geo}} + \Delta(r) + r\cos\left[\theta + \arcsin\left(\delta(r)\right)\sin(\theta)\right. \\ \left. -\zeta(r)\sin(2\theta)\right] \end{aligned} \tag{3}$$

$$Z(r,\theta) = Z_{\text{geo}} + \kappa(r)\, r\sin(\theta) \tag{4}$$

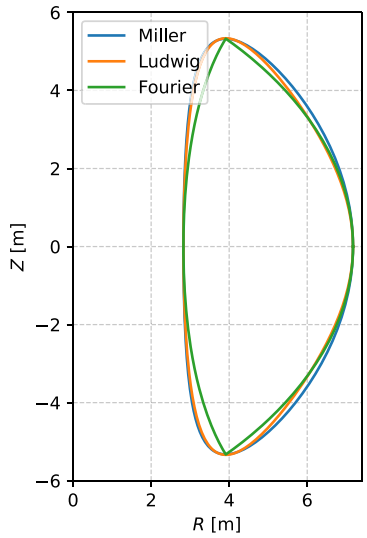

Figure 1. Examples of the plasma boundary produced by three parameterisations used in PyTok.

where R_{geo} is the geometric major radius; $\Delta(r)$ is the radial profile of the Shafranov shift, taken as $\Delta(r) = \Delta(0)\left(1 - r^2/a^2\right)$, where $\Delta(0)$ is the central Shafranov shift defined as $\Delta(0) = R_{\text{mag}} - R_{\text{geo}}$, where R_{mag} is the major radius of the magnetic axis and is approximated as $R_{\text{mag}} = R_{\text{geo}}\sqrt{1+\epsilon^2}$, where $\epsilon = 1/A$ is the inverse aspect ratio; $\delta(r)$, $\zeta(r)$, and $\kappa(r)$ are, respectively, the radial profiles of triangularity, squareness and elongation; θ is the poloidal angle, with $\theta = 0$ corresponding to the outboard midplane; and Z_{geo} is the height of the geometric centre (taken as 0 for double null plasmas). Examples of the last closed flux surface geometry for each of the three parametisations are shown in figure 1. Volume integrals are given by

$$\int_V Y(x)\frac{\text{d}V}{\text{d}x}\text{d}x \tag{5}$$

and are computed from the geometry of each nested flux surface, with elongation, $\kappa(r)$, triangularity, $\delta(r)$, squareness, $\zeta(r)$ and Shafranov shift, $\Delta(r)$.

Quasi-neutrality is imposed and the electron density profile is specified in the input. For simplicity, all species are assumed to have the same density profile. The thermal helium density is specified as a fraction of the electron density, $n_{\text{He}} = f_{\text{He}} n_{\text{e}}$. The fast helium density is small and is ignored. For impurities, one impurity species is allowed with an average charge state, Z_{imp} and mass, M_{imp} defined in the input. The effective ion charge, Z_{eff}, is also specified. The central ion density is therefore given as:

$$n_{\text{i0}} = \frac{\left(Z_{\text{eff}} - Z_{\text{imp}}\right) n_{\text{e0}} + \left(2Z_{\text{imp}} - 4\right) n_{\text{He,0}}}{1 - Z_{\text{imp}}}. \tag{6}$$

The fraction of tritium, f_{trit}, is specified, giving $n_{\text{T0}} = f_{\text{trit}}\, n_{\text{i0}}$ and $n_{\text{D0}} = \left(1 - f_{\text{trit}}\right) n_{\text{i0}}$.

2.3. Plasma fusion born alpha particles

For the higher current devices considered here fast alpha first orbit loss is negligible, however it can be important for lower

plasma currents and is included for completeness, based on an estimation from [19]. A critical plasma current for alpha confinement is defined as:

$$I_{\mathrm{crit}} = 5.436 \times 10^6 \sqrt{\epsilon}\left(\frac{1+\kappa^2}{2\kappa}\right). \tag{7}$$

The confined alpha fraction, f_α, is:

$$f_\alpha = \exp\left[-K_l\sqrt{\epsilon}\left(\frac{I_{\mathrm{crit}}}{I_{\mathrm{p}}}\right)^l\right], \text{ for } I_{\mathrm{p}} > I_{\mathrm{crit}} \tag{8}$$

$$= 1 - K_l\sqrt{\epsilon}\left(\frac{I_{\mathrm{crit}}}{I_{\mathrm{p}}}\right)^{l+1}, \text{ for } I_{\mathrm{p}} < I_{\mathrm{crit}} \tag{9}$$

where the value of l depends on the density, temperature and reactivity profiles, but is assumed fixed at $l = 3$, and K_l is a fitting parameter taken as $K_l = 0.068$. For different profiles to those used in [19] this expression may become less accurate, but is useful to include to give some indication of when first orbit alpha losses become important and to account for this effect.

The fast particle parameters are determined following the approach outlined in [20], which uses a simplified form of the Fokker–Planck equation that neglects energy diffusion, pitch-angle scattering and trapping effects but retains frictional drag and assumes a delta function fast alpha source at the alpha birth energy $E_\alpha = m_\alpha v_\alpha^2/2$:

$$\frac{\partial f}{\partial t} = \frac{1}{\tau_{\mathrm{s}} v^2}\frac{\partial}{\partial v}\left(v^3 + v_{\mathrm{c}}^3\right) f + \frac{S_0}{4\pi v_\alpha^2}\delta\left(v_\alpha - v\right) = 0 \tag{10}$$

where τ_{s} is the fast particle slowing down time, given by,

$$\tau_{\mathrm{s}} = \frac{3}{16\sqrt{\pi}}\frac{m_{\mathrm{e}} m_\alpha v_{\mathrm{e}}^3}{Z_\alpha^2 e^4 n_{\mathrm{e}} \ln\Lambda} \tag{11}$$

the critical velocity, v_{c}, is

$$v_{\mathrm{c}} = \left(\frac{3\sqrt{\pi} m_{\mathrm{e}}}{4 m_\alpha} Z_{\mathrm{i}}\right)^{1/3} v_{\mathrm{e}} \tag{12}$$

and the fast particle source, S_0, is

$$S_0 = n_{\mathrm{D}} n_{\mathrm{T}} \langle\sigma v\rangle_{\mathrm{DT}} \tag{13}$$

where $v_{\mathrm{e}} = \sqrt{2 k_{\mathrm{B}} T_{\mathrm{e,[K]}}/m_{\mathrm{e}}} = 1.88 \times 10^7 \sqrt{T_{\mathrm{e,[keV]}}}$ is the electron thermal velocity, $\ln\Lambda$ is the Coulomb logarithm [21] and $\langle\sigma v\rangle_{\mathrm{DT}}$ is calculated with the Bosch-Hale reactivity coefficients [22]. As defined in [20] the fast alpha density is given by:

$$n_\alpha = S_0 \tau_{\mathrm{s}} I_2\left(\frac{v_{\mathrm{c}}}{v_\alpha}\right) \tag{14}$$

and the pressure is:

$$p_\alpha = \frac{1}{3}\langle m_\alpha v^2\rangle_{\mathrm{s}} = \frac{2 I_4}{3 I_2} n_\alpha E_\alpha$$
$$= \frac{2}{3} S_0 \tau_{\mathrm{s}} I_4\left(\frac{v_{\mathrm{c}}}{v_\alpha}\right) E_\alpha \tag{15}$$

where,

$$I_2(a) = \frac{1}{3}\left(\frac{1+a^3}{a^3}\right) \tag{16}$$

$$I_4(a) = \frac{1}{2} - a^2\left[\frac{1}{6}\ln\left(\frac{1-a+a^2}{(1+a)^2}\right) + \frac{1}{\sqrt{3}}\left(\tan^{-1}\left(\frac{2-a}{a\sqrt{3}}\right) + \frac{\pi}{6}\right)\right]. \tag{17}$$

It is assumed that the alpha particles thermalise on the flux surface they are born on allowing the above expression to be evaluated as a function of the chosen radial coordinate. For simplicity, it is assumed that all species have the same density profile shape and the volume average of equation (14) is used to define the fast alpha density profile. The thermal helium density is taken as a fraction of the electron density, typically between 5%–10%.

2.4. Plasma power balance

Global power balance is imposed and the plasma is assumed to be in steady-state:

$$P_{\mathrm{in}} = P_{\mathrm{out}} \tag{18}$$

$$P_{\mathrm{H\&CD}} + f_\alpha P_\alpha + P_{\mathrm{OH}} = P_{\mathrm{rad}} + \frac{W_{\mathrm{th}}}{\tau_{\mathrm{E}}} \tag{19}$$

where τ_{E} is the energy confinement time and P_{rad} is calculated using a general formula for radiation loss assuming the plasma is in coronal equilibrium [23]:

$$P_{\mathrm{rad}}(T_{\mathrm{e}}) = n_{\mathrm{e}} n_{\mathrm{imp}}\left(1 + 3.0 T_{\mathrm{e}}\right) \times 10^{-43} Z_{\mathrm{imp}}^{(3.7 - 0.33\ln T_{\mathrm{e}})} \tag{20}$$

where T_{e} is the electron temperature in keV and the radiated power density has units MW m^{-3}. The expression includes bremsstrahlung and line radiation but cyclotron emission is neglected.

A range of energy confinement time scalings, having the general form:

$$\tau_{\mathrm{E,scaling}} = C_{\tau_{\mathrm{E}}} I_{\mathrm{p}}^{\alpha_{I_{\mathrm{p}}}} B_{\mathrm{T}}^{\alpha_{B_{\mathrm{T}}}} P_{\mathrm{L}}^{\alpha_{\mathrm{P}}} n^{\alpha_n} R^{\alpha_R} \epsilon^{\alpha_\epsilon} \kappa^{\alpha_\kappa} M^{\alpha_M} \tag{21}$$

are included and are summarised in table 1. An energy confinement time radiation correction [24] is included where the fraction of the radiated power included on the right hand side of equation (19) and fraction of radiated power included in the confinement time definition can be varied such that the power balance expression, equation (19), becomes

$$P_{\mathrm{in}} = P_{\mathrm{H\&CD}} + f_\alpha P_\alpha + P_{\mathrm{OH}} \tag{22}$$

$$= \gamma P_{\mathrm{rad}} + \frac{W_{\mathrm{th}}}{\left(P_{\mathrm{in}} - \chi P_{\mathrm{rad}}\right)^{\alpha_{\mathrm{P}}} H f_{\tau_{\mathrm{E}}}\left(I_{\mathrm{p}}, B_{\mathrm{T}}, n, R, A, \kappa, M\right)} \tag{23}$$

where the energy confinement time has been replaced by the chosen scaling and the power term separated such that $f_{\tau_{\mathrm{E}}}$ captures all other dependencies of the scaling law and H is the confinement enhancement factor, $H = \tau_{\mathrm{E}}/\tau_{\mathrm{E,scaling}}$.

Table 1. Energy confinement time scalings. Where no coefficient is shown the scaling did not include that parameter dependence.

Scaling	C_{τ_E}	α_{I_p}	α_{B_T}	α_P	α_n	α_R	α_ϵ	α_κ	α_M
ITER98(y,2)	0.1445	0.93	0.15	−0.69	0.41	1.97	0.58	0.78	0.19
Petty08 [25]	0.1086	0.75	0.30	−0.47	0.32	2.09	0.84	0.84	
Globus [26]	0.2948	0.53	1.05	−0.58	0.65	2.66		0.78	
NSTX-Buxton [27]	0.1872	0.54	0.905	−0.38	−0.05	2.14			

To determine if the plasma is in H or L-mode the LH power threshold is calculated using the Takizuka scaling which accounts for aspect ratio and effective charge [28]:

$$P_{\mathrm{LH}} = 0.072 n_{\mathrm{e},20}^{0.7} |B_{\mathrm{out}}|^{0.7} S_{\mathrm{LCFS}}^{0.9} \left(\frac{Z_{\mathrm{eff}}}{2}\right)^{0.7} \times \left(\frac{0.1A}{1-\left(2/(1+A)^{0.5}\right)}\right) \tag{24}$$

where S_{LCFS} is the surface area of the last closed flux surface, and where $|B_{\mathrm{out}}|$ is the absolute magnetic field at the outer equatorial mid-plane, given by:

$$|B_{\mathrm{out}}| = \left(B_{\mathrm{T,out}}^2 + B_{\mathrm{p}}^2\right)^{0.5} \tag{25}$$

The toroidal field component is:

$$B_{\mathrm{T,out}} = \frac{B_{\mathrm{T}} R_{\mathrm{geo}}}{(R_{\mathrm{geo}} + a)} \tag{26}$$

and the poloidal field is:

$$B_{\mathrm{p}} = \frac{\mu_0 I_{\mathrm{p}}}{L_{\mathrm{p}}} \tag{27}$$

where I_{p} is expressed in amps and L_{p} is the poloidal circumference of the plasma calculated from the fixed boundary representation.

2.5. Plasma current balance

Along with power balance, the plasma must also be in current balance:

$$I_{\mathrm{p}} = I_{\mathrm{BS}} + I_{\mathrm{CD}} + I_{\mathrm{OH}} \tag{28}$$

where I_{BS} is the bootstrap current, I_{CD} is the auxiliary non-inductive current drive and I_{OH} is the auxiliary inductive current drive. The bootstrap current fraction, $f_{\mathrm{BS}} = I_{\mathrm{BS}}/I_{\mathrm{p}}$, can be approximated using several scalings, which have the general form $f_{\mathrm{bs}} \sim \sqrt{\epsilon}\beta_{\mathrm{p}}$, where β_{p} is the poloidal beta, defined as $\beta_{\mathrm{p}} = 2\mu_0\langle p\rangle/B_{\mathrm{p}}^2$. It is not always explicitly stated in the scalings, but it is assumed that only the thermal component of the pressure contributes to the bootstrap current, such that $p = p_{\mathrm{thermal}}$.

Several expressions for the bootstrap fraction, f_{BS} are available but equation (20) of [29] has been adopted as the default and is used throughout the subsequent analysis:

$$f_{\mathrm{BS}} = 0.234\epsilon^{0.5}\beta_{\mathrm{p}} c_{\mathrm{p}}^{0.8} \tag{29}$$

where c_{p} is a pressure peaking factor. A bootstrap modifier can be input to adjust this parameter, since the entire plant power balance and cost is sensitive to the value.

For the flat-top, only electron cyclotron external current drive is considered, and the current is calculated using a normalised current drive efficiency, η_{CD}:

$$I_{\mathrm{CD}} = 0.031\eta_{\mathrm{CD}} \frac{T_{\mathrm{e,keV}}}{R_{\mathrm{geo}} n_{\mathrm{e},20}} P_{\mathrm{CD}} \tag{30}$$

with $\eta_{\mathrm{CD}} = 0.30$ based on comparison with dedicated modelling [30].

The auxiliary inductive current can be specified as a fraction of the total current. The loop voltage required to drive this current is, $V_{\mathrm{loop}} = f_{\mathrm{ind}} I_{\mathrm{p}} \mathcal{R}$, where the plasma resistance is [31]

$$\mathcal{R} = 2.15 \times 10^{-9} \times (4.3 - 0.6A) \frac{Z_{\mathrm{eff}} R_{\mathrm{geo}}}{\kappa a^2 \left(T_{\mathrm{e}}/10\right)^{3/2}} \tag{31}$$

If the EC current drive power is specified, or inductive current drive fraction is given, then the loop voltage is used to estimate the flat-top duration. Although generally small, if auxiliary inductive current drive is used the ohmic power produced in the plasma, $P_{\mathrm{OH}} = V_{\mathrm{loop}} I_{\mathrm{p}}$ is added to the power balance expression, equation (19).

The flux required to ramp-up the plasma is:

$$\Phi_{\mathrm{total}} = \Phi_{\mathrm{p,ind}} + \Phi_{\mathrm{res}} \tag{32}$$

The inductive component is given by, $\Phi_{\mathrm{p,ind}} = L_{\mathrm{p}} I_{\mathrm{p}}$, where L_{p} is the plasma self-inductance, which has an internal, $L_{\mathrm{p,int}}$ and external, $L_{\mathrm{p,ext}}$ component, such that $L_{\mathrm{p}} = L_{\mathrm{p,int}} + L_{\mathrm{p,ext}}$. The internal component is:

$$L_{\mathrm{p,int}} = \frac{1}{2}\mu_0 R_{\mathrm{mag}} l_{\mathrm{i}} \tag{33}$$

where l_{i} is the plasma internal inductance. For the external component, an expression that includes a low aspect ratio correction is given in [32] as:

$$L_{\mathrm{p,ext}} = \mu_0 R_{\mathrm{mag}} \left(\frac{f_1(\epsilon)(1-\epsilon)}{(1-\epsilon) + f_2(\epsilon)\kappa}\right) \tag{34}$$

where:

$$f_1(\epsilon) = \left(1 + 1.81\sqrt{\epsilon} + 2.05\epsilon\right) \ln\left(\frac{8}{\epsilon}\right) - \left(2.0 - 9.25\sqrt{\epsilon} - 1.21\epsilon\right) \tag{35}$$

$$f_2(\epsilon) = 0.73\sqrt{\epsilon}\left(1 + 2\epsilon^4 - 6\epsilon^5 + 3.7\epsilon^6\right) \tag{36}$$

The resistive component is given by:

$$\Phi_{\rm res} = C_{\rm Ejima}\,\mu_0 R_{\rm geo} I_{\rm p} \tag{37}$$

where $C_{\rm Ejima}$ is the Ejima coefficient, which varies with ramp rate and other parameters [33], and is an input variable, with default value $C_{\rm Ejima} = 0.4$ used in this analysis. Detailed analysis of the plasma ramp-up [34] has found that values as low as $C_{\rm Ejima} \approx 0.2$ may be achievable with early H-mode access and sufficient heating during the ramp-up.

2.6. Plasma stability and power exhaust

To evaluate plasma stability, several metrics are calculated:

$$\beta_{\rm T} = \frac{\langle p \rangle}{B_{\rm T}^2/2\mu_0} \tag{38}$$

$$\beta_{\rm p}\,(1) = \frac{\langle p \rangle}{B_{\rm p}^2/2\mu_0} \tag{39}$$

$$\beta_N = \beta_{\rm T}\,(\%)\,\frac{aB_{\rm T}}{I_{\rm p,[MA]}} \tag{40}$$

$$I_N = \frac{I_{\rm p,[MA]}}{aB_{\rm T}} \tag{41}$$

$$q_{cycl} = \frac{5\kappa\epsilon^2 R_{\rm geo} B_{\rm T}}{I_{\rm p,[MA]}} \tag{42}$$

$$q_* = \frac{5\epsilon^2\left(1+\kappa^2\right) R_{\rm geo} B_{\rm T}}{2 I_{\rm p,[MA]}} \tag{43}$$

$$q_{95} = \frac{5\left(1+\kappa^2\right)}{2\,(A-1)\,I_N} \tag{44}$$

For values of β, the total value and separate thermal and fast particle components are calculated. Limits of stability are:

$$\beta_{\rm N,no-wall} = 3.12 + 3.5\epsilon^{1.7} \tag{45}$$

$$\beta_{\rm p,no-wall} = \frac{0.275^{2/3}\left(AI_N q_{95}\right)^{0.5}}{I_N^{2/3}} \tag{46}$$

$$n_{\rm GW} = \frac{I_{\rm p,[MA]}}{\pi a^2} \tag{47}$$

$$\kappa_{\rm max} = 2.4 + 65e^{-A/0.376} \tag{48}$$

The expression for the $\beta_{\rm N,no-wall}$ is taken from [35]. For the typical operating points considered here with high bootstrap fractions, elevated minimum safety factor ($q_{\rm min} > 2$ to avoid sawteeth and the lowest order neoclassical tearing modes), and low internal inductance ($l_i < 0.5$), it was found that an ideal MHD external $n = 1$ kink mode, with stability properties similar to those of the peeling-ballooning modes that typically limit the pedestal pressure, sets a limit on the achievable global poloidal beta ($\beta_{\rm p}$). An empirical scaling for this limit, $\beta_{\rm p,no-wall}$ was derived and is given above [36]. The density at the pedestal top is compared to the Greenwald limit and an empirical scaling for the maximum achievable plasma elongation is taken from [37]. For each limit there is an input parameter that defines how close to the limit the plasma operating point should be:

$$C(\beta_N) = \beta_N/\beta_{\rm N,no-wall} \tag{49}$$

$$C(\beta_{\rm p}) = \beta_{\rm p}/\beta_{\rm p,no-wall} \tag{50}$$

$$f_{\rm GW} = n_{\rm e,ped}/n_{\rm GW} \tag{51}$$

$$C(\kappa) = \kappa/\kappa_{\rm max} \tag{52}$$

For the plasma exhaust, the peak heat flux at the divertor target is calculated as

$$q_{\rm peak} = \frac{P_{\rm SOL}\,(1 - f_{\rm rad,SOL}) f_{\rm c} \sin\left(\theta_{\rm plate}\right)}{2\pi R_{\rm strike} N_{\rm div} f_x \lambda_q} \tag{53}$$

where $P_{\rm SOL}$ is the conducted power entering the scrape-off layer and $N_{\rm div}$ is the number of divertors (single or double null). $f_{\rm rad,SOL}$ is the fraction of $P_{\rm SOL}$ that that is radiated in the scrape-off layer, $f_{\rm c}$ is the fraction of the power going to the inner or outer divertor, $\theta_{\rm plate}$ is the poloidal angle between the divertor leg and the divertor surface and $f_{\rm x}$ is the poloidal flux expansion. $R_{\rm strike}$ is the absolute geometric radius of the strike point on the divertor surface. This can be set by the user directly or calculated by projecting a user-defined poloidal leg length from the X-point using the geometric curvature of the last closed flux surface. Finally, λ_q is calculated from scaling laws [38, 39]

$$\lambda_{\rm q,Eich15} = 1.35 \times 10^{-3} P_{\rm SOL}^{-0.02} R_{\rm geo}^{0.04} B_{\rm p,out}^{-0.92} \epsilon^{0.42} \tag{54}$$

$$\lambda_{\rm q,MASTB} = 1.84 \times 10^{-3} P_{\rm SOL}^{0.18} B_{\rm p,out}^{-0.68} \tag{55}$$

$$\lambda_{\rm q,MASTI} = 4.57 \times 10^{-3} P_{\rm SOL}^{0.22} I_{\rm p}^{-0.64} \tag{56}$$

Simplified divertor power loading metrics are also calculated, with $P_{\rm SOL}/R_{\rm geo}$ used most frequently.

2.7. Plasma design point evaluation

A typical plasma simulation requires the user to define the plasma geometry, kinetic profiles, toroidal field and value of $H_{\rm ITER98(y,2)}$. The code scans the plasma current to find solution(s) with the specified energy confinement enhancement factor; there may be several, but only the solution with the highest $I_{\rm p}$ has $f_{\rm BS} < 1.0$ and is chosen. Operating points with $f_{\rm BS} > 1$ are still valid, but require auxiliary power to drive counter-current, so are discarded. The process is illustrated in figure 2 where it can be seen that there are multiple possible values of plasma current for $H_{\rm ITER98(y,2)} = 1.4$, but only one lies to the right of the ignition line, so it is chosen as the self-consistent operating current.

Where there is a fusion power target for a specified plasma geometry the plasma class implements the minimise function from the Scipy package [40] to explore the density, temperature and $Z_{\rm eff}$ space to find a solution that provides the target power, while respecting the stability, density and divertor power loading constraints imposed by the user. The method is an automated equivalent to navigating through a (n,T) POPCON plot with the $Z_{\rm eff}$ dimension added to modify the divertor power loading metric. Figure 3 shows an example POPCON plot for fixed $H_{\rm ITER98(y,2)} = 1.4$, with a operating point shown by the red star at the target fusion power of $\rm P_{fusion} = 1600$ MW, that respects the operational constraints of

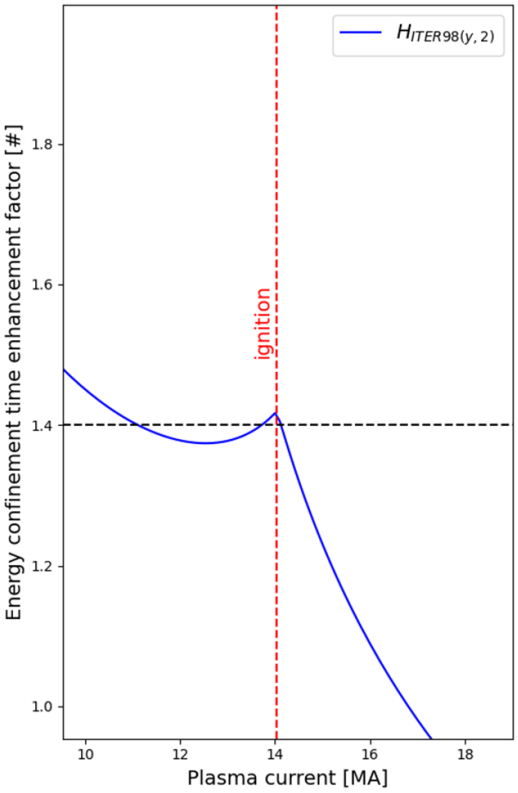

Figure 2. Illustration of the method used to find the plasma current that meets the assumed energy confinement time of $H_{\mathrm{ITER98(y,2)}} = 1.4$. The red dashed line represents the point where the plasma is ignited and $f_{\mathrm{BS}} = 1$. To the left of this line $f_{\mathrm{BS}} > 1$ and the auxiliary power is driving a negative current. Any solutions in this region are discarded.

$P_{\mathrm{SOL}}/R_{\mathrm{geo}} = 25\,\mathrm{MW\ m^1}, f_{\mathrm{GW}} = 1.0$ and $C(\beta_N) < 1.0$; demonstrating that the optimiser is effective at identifying the best point within the 3-dimensional parameter space.

2.8. Central solenoid

The flux swing, Φ_{CS} required from the central solenoid at the plasma can be calculated by the plasma class, or specified by the user. The method described in [13] is used to calculate the total flux swing from $-\phi_{\mathrm{premag}}$ to $+\phi_{\mathrm{premag}}$,

$$\Phi_{\mathrm{premag}} = \pi B_{\mathrm{CS}} R_{\mathrm{avg}} \left[1 - \frac{t}{R_{\mathrm{avg}}} + \frac{t^2}{3R_{\mathrm{avg}}^2}\right] \tag{57}$$

where t is the radial thickness and R_{avg} is the radial midpoint of the solenoid. The outer radius is incremented and the inner radius calculated using the magnetic field in the bore, B_{CS} and the average current density across the winding, J_{CS} by

$$R_{\mathrm{min}} = R_{\mathrm{max}} - \frac{B_{\mathrm{CS}}}{\mu_0 J_{\mathrm{CS}}} \tag{58}$$

until the flux swing reaches the target value. It was assumed that the central solenoid would be wound from ReBCO high-temperature coated superconductor, a core technology domain for TE. The magnetic field in the bore, B_{CS} was set to 18 T, which was considered feasible from the engineering perspective. Further details on magnet engineering and the integrated plasma-magnet workflow can be found in [41].

2.9. Toroidal field magnet system

The engineering model for the TF magnet system is based on ReBCO high-temperature coated superconductor (HTS). The design assumes HTS tapes are soldered into copper channels which are non twisted, to take advantage of the field-angle dependence of the critical current and maximise the current density. A single winding is sandwiched between electro-thermal interface (ETI) plates and an even number of windings are assembled side-by-side in the winding pack, therefore the width of the coil in the toroidal direction is discretised. Figure 4 outlines the dimensions used in a cross-section of one TF pack. The inner radius of the winding pack is given by:

$$R_{\mathrm{pack,min}} = \frac{N_{\mathrm{limbs}}}{2\pi} \times [N_{\mathrm{windings}} W_{\mathrm{cable}} + (N_{\mathrm{windings}} + 1) W_{\mathrm{ETI}} + 2W_{\mathrm{case}}] \tag{59}$$

where by convention W_n is the width of component n in the toroidal direction. R_{min} has a minimum value for $N_{\mathrm{windings}} = 2$ for a given number of limbs. If a central solenoid is present then the minimum value becomes the outer radius of the solenoid. A radial offset for the TF case is calculated iteratively based on in-plane stress analysis, described in a subsequent section.

The outer radius of the winding pack in the core, $R_{\mathrm{pack,max}}$ is determined by iteration, based on several engineering feasibility considerations. First, there must be sufficient space available for the number of tapes required to carry the current, the copper channels and insulation between turns (if required). The current that must flow through the superconducting core is fixed and determined by the magnetic field required at the geometrical major radius of the plasma:

$$I_{\mathrm{core}} = \frac{2\pi B_0 R_{\mathrm{geo}}}{\mu_0} \tag{60}$$

therefore a single winding pack must have sufficient area in the horizontal plane to accommodate current I_{core}/N_{limbs}. The engineering critical current density and tape thickness is a user input to PyTok and is used to calculate the current carrying capacity of a single tape. A factor is applied to account for radiation-induced degradation of the critical current throughout the lifetime of the magnet. A typical value of $\gamma_0 = I/I_{c0}$ is 0.3 to allow a two-fold reduction in performance while maintaining operating margin. The configuration fails if,

$$T_{\mathrm{pack}} < \left(\frac{I_{\mathrm{core}}}{N_{\mathrm{limbs}} N_{\mathrm{windings}} \gamma_0 J_{\mathrm{eng}} W_{\mathrm{tape}}}\right) + N_{\mathrm{turns}} (T_{\mathrm{insulation}} + T_{\mathrm{cable}}) \tag{61}$$

where by convention T_n is the length of component n in the radial direction.

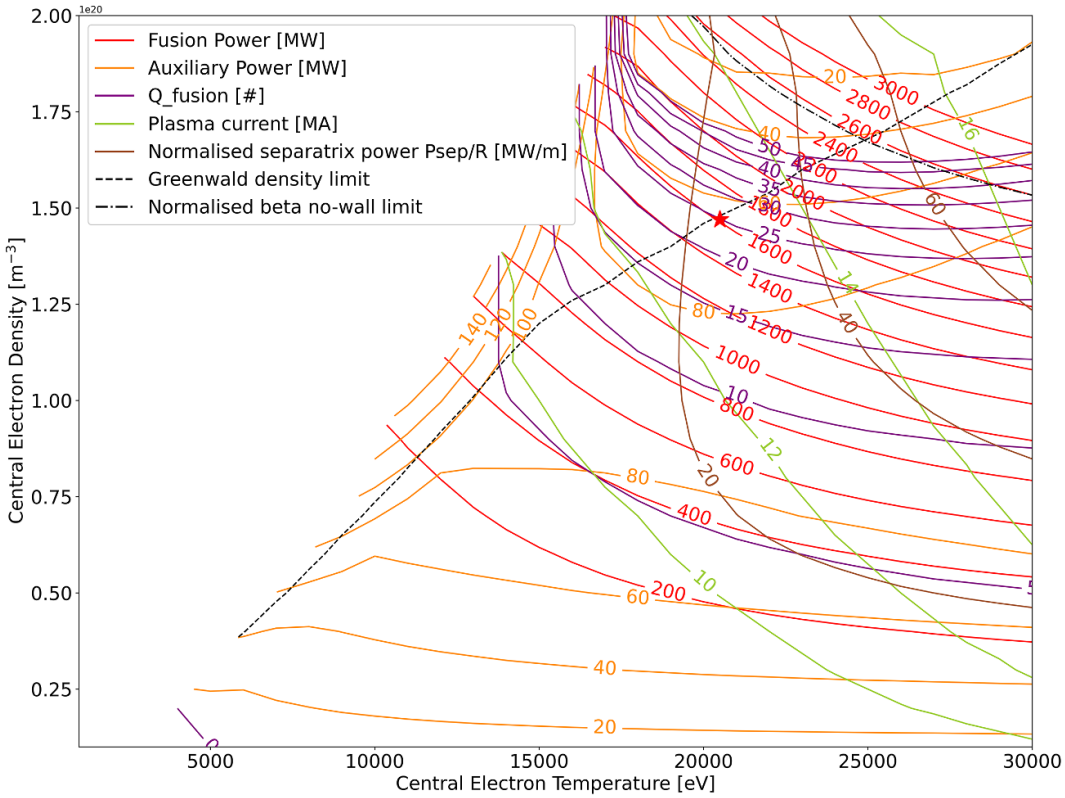

Figure 3. Example of plasma operating point contours (POPCON) produced by PyTok for fixed $H_{\mathrm{ITER98(y,2)}} = 1.4$. The optimum operating point with the target fusion power of $\mathrm{P_{fusion}} = 1600$ MW that satisfied the operational limits of $P_{\mathrm{SOL}}/R_{\mathrm{geo}} = 25\,\mathrm{MW\ m^{-}1}$, $f_{\mathrm{GW}} = 1.0$ and $\beta_N < \beta_{N,no-wall}$, is marked with a red star. The optimisation explores the density, temperature and Z_{eff} space to find a solution that provides the target fusion power, while respecting stability, density and normalised exhaust power constraints. The POPCON is plotted with constant Z_{eff} at the value found by the optimiser.

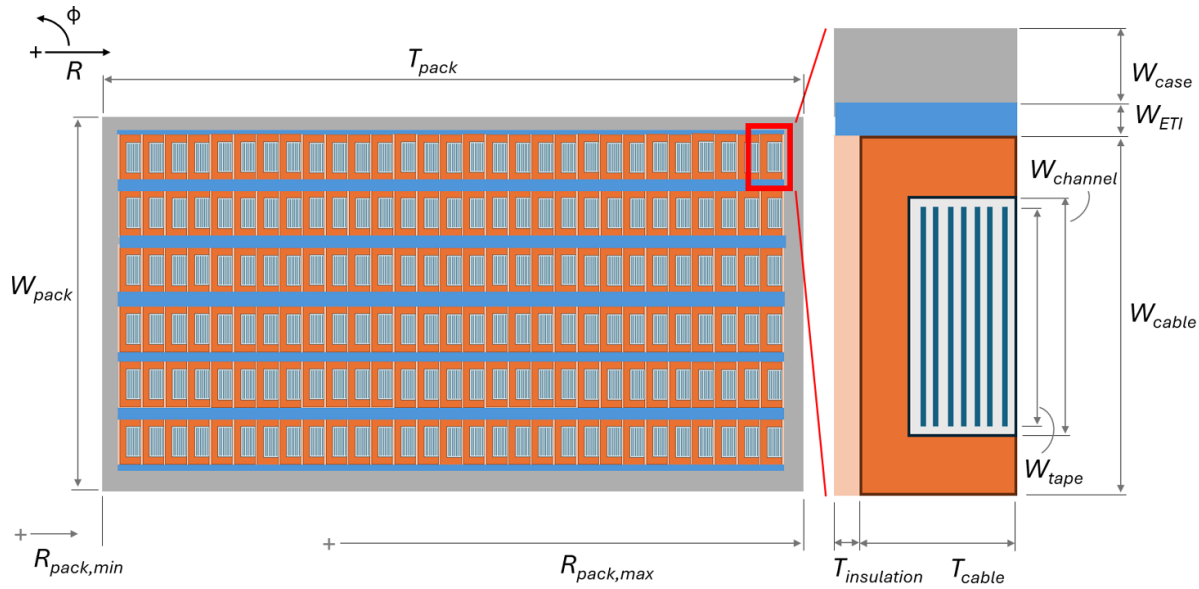

Figure 4. An outline of the dimensions used to build the TF coils. The left figure shows the cross section of an entire TF pack with six pancakes, and the right figure shows a zoomed-in view of one copper u-channel with ETI plate and casing. Note that the figure and sub-components are not to scale.

The second feasibility criterion is that the maximum background field on the conductor:

$$B_{\text{peak}} = \frac{\mu_0 I_{\text{core}}}{2\pi R_{\text{pack,max}}} \tag{62}$$

is less than a user defined value, with a default of 20 T.

The third feasibility requirement is the quench safety of the system. The coil set must be able to absorb its magnetic stored energy internally during a quench without the average temperature of the coils exceeding a limit defined by an input value, default 200 K. Modelling by TE indicates that this limit should enable hot spot temperatures to be kept below 400 K, thus avoiding damage to the coil. To achieve this, the magnetic stored energy in the winding pack must be balanced by the energy required to increase its temperature from the operating temperature, nominally 20 K, to the user-defined average quench temperature. The stored energy is calculated with:

$$E_{\text{mag}} = \frac{\pi}{\mu_0} B_0^2 R_{\text{geo}}^2 \oint \frac{z}{r} \hat{\underline{r}}.d\underline{l} \tag{63}$$

The coil profile is described by a list of r, z coordinates so the line integral is evaluated numerically using the mid-point 2nd order rule:

$$\oint \frac{z}{r} \hat{\underline{r}}.d\underline{l} = \sum_i \frac{z_{i+1} + z_i}{r_{i+1} + r_i} (r_{i+1} - r_i) \tag{64}$$

The method has been verified using the 3D magnet modelling tool RAT [42] with an error $< 5\,\%$. The coil shape, width, W_{pack} and thickness, T_{pack} is used to calculate the mass of the winding pack and the specific heat capacity of copper is integrated between the operating temperature and the average quench temperature to obtain the quench energy. If the stored energy exceeds the quench energy then the configuration is considered unfeasible.

The final feasibility check is the in-plane stress in the winding pack and case at the mid-plane. The method implemented in PROCESS [43] was adopted for this calculation assuming a bucked-wedged hybrid configuration [44], with 3 layers representing the central solenoid, steel case and winding pack. The maximum Von Mises stress is compared with a user input or default 667 MPa with a safety factor of 1.5 due to the low maturity of the structural design. The configuration fails if the stress limit is breached.

The 2D shape of a TF magnet coil can be specified as either a Princeton-D or a picture frame, with the latter having separate free parameters for the radius of curvature on the high-field side and low-field side corners. The height (length along tokamak axis) of the coil is determined from the plasma geometry combined with a placeholder divertor topology and blanket structures behind the divertor cassette. The radius of the return leg is determined either by a user defined toroidal field ripple (default value 0.3%) or by the toroidal width required to remove a segment of the tokamak (if required by the maintenance scheme). Both the height and return leg radius can have a significant impact on the stored magnetic energy in the coil, thus affecting the value of $R_{\text{pack,max}}$ and should not be neglected when assessing the feasibility of the radial build.

For further details of magnet engineering and the integrated plasma-magnet workflow please refer to [41].

2.10. Centre column structures

With the central solenoid and toroidal-field magnet winding pack and case defined, the remaining radial space between $R_{\text{pack,max}}$ and the last closed flux surface of the plasma is allocated to the vacuum gap between the plasma and first wall, the first wall itself, the blanket, the vacuum vessel, and thermal/vacuum insulation between the vessel and magnet system. The structures and gaps are defined by the user as a list of layers, with each layer consisting of a name, thickness, material, density and half-value layer (HVL) for fast neutron attenuation. The HVL is defined as the thickness of material over which the intensity (flux) of a beam of radiation decreases by 50%. During the radial build the thickness of some layers are adjusted so that the structure as a whole fits within the available space. The first-wall structures—armour and heatsink—are fixed, as are the vacuum vessel components, because the primary function of these elements is neither shielding nor tritium breeding, thus the thicknesses are specified by other considerations. If the available space in the centre column is less than the reserved space then the radial build fails. With a structural configuration that fits within the radial envelope, the HVL and thickness of each layer are used to calculate the cumulative attenuation of the first-wall fast neutron flux. The flux incident on layer $i+1$ is,

$$\phi_{i+1} = \frac{\phi_i}{2^{(T_i/\text{HVL}_i)}} \frac{r_i}{r_{i+1}} \tag{65}$$

where the second term accounts for the increase in flux due to the linear reduction in the surface area of the cylinder representing each layer, since $r_{i+1} < r_i$. The incident neutron flux from the plasma is taken as the total neutron production rate divided by the first-wall surface area, multiplied by a factor of 2 to estimate the peak value at the mid-plane. A factor of 12 is applied to the flux transmitted through the final layer to account for build-up of lower-energy neutrons (factor 6) and back-scattering within the TF winding pack and case (factor 2). The HVL for each material was calculated in isolation using an infinite slab geometry in the Monte Carlo radiation transport code described in section 2.14, and the reduced model was verified across a range of radial builds using full 3D geometries. The principal limitation of the method is the single group treatment, where the HVL is calculated based on the transmitted fast ($E_{\text{n}} > 0.1$ MeV) neutron flux from incident 14.1 MeV neutrons. Hong *et al* [45] overcame this limitation by coupling a tokamak system code with a 1D discrete ordinates code [46] to solve the multi-group Boltzmann transport equation. While this would be advantageous for exploring a small parameter space in greater detail, PyTok was developed as a low-fidelity tool capable of large parameter sweeps, with the radial build iterated several times for a single design point, therefore the lower-fidelity single group treatment verified with high-fidelity radiation transport codes was preferred for this implementation.

The final transmitted flux is used to estimate the lifetime of the TF magnet based on degradation of the critical current. A polynomial fit to the the data from figure 5 of [47] was used to estimate the degradation of critical current as a function of neutron fluence; for YBCO with artificial flux pinning centres the function is,

$$I_{c,t} = I_{c,0}\left(1 + 0.02\Phi_n - 0.38\Phi_n^2 + 0.17\Phi_n^3 - 0.02\Phi_n^4\right) \quad (66)$$

The point where $\gamma_t = I/I_{c,t} \geqslant \gamma_{\max}$, a user defined variable (default 0.7), defines the lifetime fluence of the TF magnet, which sets the life of the plant. It is recognised that displacement damage is generally a better metric than fluence for degradation of critical current, however in YBCO exposed to a neutron fluence with negligible thermal contribution fast fluence is an adequate proxy.

2.11. Thermal power extraction

PyTok has separate primary coolant loops for the outboard first wall, outboard blanket volume, divertor, inboard (center column) first wall and inboard blanket (shield) volume. The heat deposited in the blanket/shield behind the divertor cassette is assumed to be extracted by the inboard blanket loop. The Pyfluids Python package [48] is used for fluid properties at different points in the loop. The fluid, minimum and maximum cycle pressures, the inlet and outlet temperatures of the heater, and the isentropic efficiency of the compressor/pump are parameters set by the user for each loop. For each loop the power transferred to the secondary cycle, the power rejected and the compressor/pumping power are calculated based on the input parameters and the heating power.

For the volumetric heating the power is taken from an input parameter that gives the fraction of the total neutron energy deposited in the component, based on Monte Carbo radiation transport calculations described in section 2.14, therefore an iterative process is required for greatest accuracy. For the first wall components the heating power is the total radiated power from the plasma divided such that 20% is incident on the inboard wall and 80% on the outboard wall. The divertor is assumed to take all of the power conducted into the scrape-off layer. There is also a neutron component for each of the plasma-facing surfaces to account for the finite thickness of the engineered surface and heatsink, but these are small fractions of the total (2%–5%).

2.12. Power conversion

High efficiency power conversion/generation cycles are complex systems, therefore high-level parameters are used to represent them. It is assumed that the power conversion technology will be a steam Rankine cycle due to the high maturity and commercial availability of the plant equipment. A study by Manchester University was commissioned by TE to produce thermal—electric conversion efficiencies for 4 configurations, shown in table 2.

The cycle efficiency was further modified to account for the power required for ultimate heat rejection:

- evaporative cooling tower in cold ($\lesssim 20°$) ambient conditions, –3%
- evaporative cooling tower in hot ($\gtrsim 30°$) ambient conditions, –5%
- dry cooling tower in cold ambient conditions, –5%
- dry cooling tower in hot ambient conditions, –7%

Discharge to a body of water has no power requirement and is the most efficient heat sink, but has potential environmental consequences, especially in rivers or lakes, and siting constraints.

2.13. 3D model generation

The Python application programming interface (API) for FreeCAD [8] was used to convert 2D profiles and internal engineering parameters into a CAD model for visualisation and use by higher fidelity codes requiring 3D geometries. The parametric model generation ensures that clash free, watertight solid representation is produced, which is compatible with radiation transport codes. The volume of each component together with its material is stored and passed in memory to the cost estimator tool, ensuring that changes to the reactor configuration are accurately reflected in the cost model. Figure 5 shows an example of the CAD generated by PyTok, rendered in Paraview [49]. The tool does not have the versatility of codes such as Paramak [50], but is tailored to the TE concept and workflow.

2.14. Radiation transport

PyTok used the 3D model and plasma parameter set to automatically generate inputs for an in-house neutronics tool based on the Geant4 toolkit [51–53], which enabled nuclear effects to be considered at the earliest stage of each design loop. Surface mesh descriptions of components in STL format are directly imported by G4Tokamak to calculate component level heating data and tritium breeding ratios within ∼1 h of a design point being identified for analysis. A volume mesh of the entire 3D model is also automatically generated with the GMSH [54] Python API, which is combined with an automatic iterative variance reduction technique [55] to assess the global distribution of radiation effects, with minimal user intervention in a few node days (see figure 6 for an example output).

2.15. Cost models

Chapman highlights the importance of incorporating cost estimates as a key performance measure in the early design phases of fusion power plants, because it is a novel technology entering a mature energy market [56]. Any commercial project must consider the value of the product that is being developed to determine whether the investment is justified, in the context of competitiveness with conventional technologies in the market. PyTok includes cost models both to identify cost drivers and to estimate the commercial value of the end product, a metric which is frequently omitted from comparable analyses. It is acknowledged that the estimate is likely to be highly uncertain

Table 2. Steam Rankine Cycle performance estimates for different temperature fluids for blanket and divertor, and divertor heat utilisation.

Divertor In/Outlet (°C)	Blanket In/Outlet (°C)	Divertor Utilisation (%)	Efficiency (MWe/MWt)
100/125	350/450	50	0.360
100/150	400/500	59	0.376
200/250	450/600	100	0.442
300/350	550/750	100	0.509

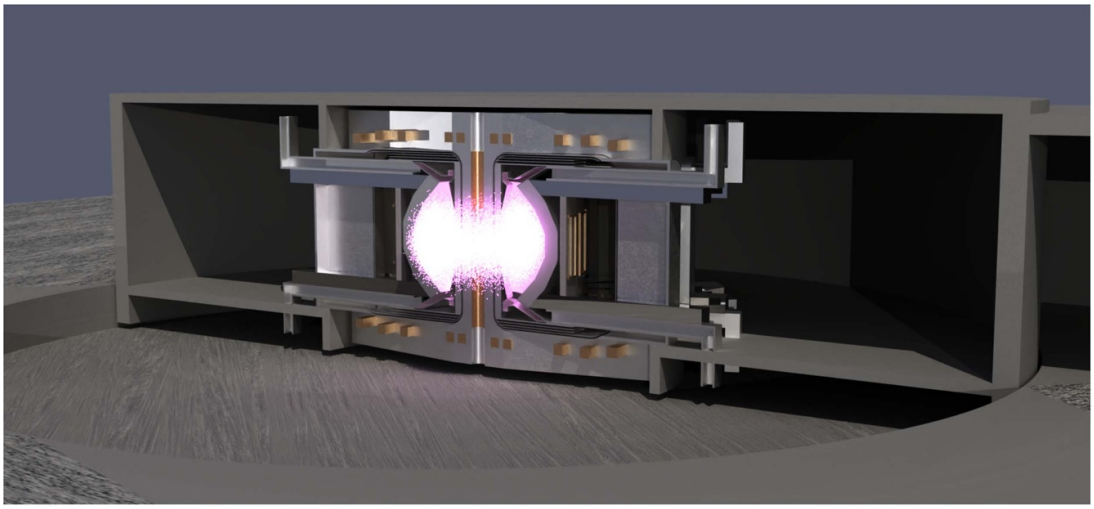

Figure 5. Example of geometry built with PyTok 3D modeller, rendered in Paraview.

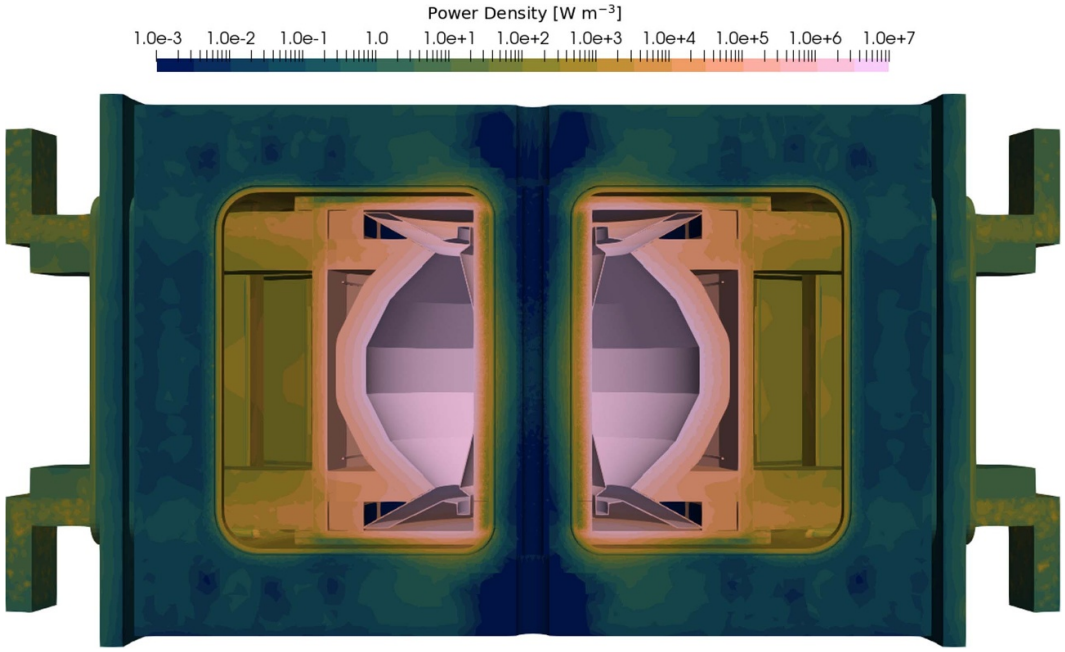

Figure 6. Example of neutronics results from PyTok generated 3D model with G4Tokamak radiation transport.

due to the novel technologies involved, the complexity of the system, and the low maturity of the design [57]. Nevertheless, an early estimate can be used to indicate whether the cost represents an efficient use of capital and to guide design decisions and prioritisation of technology development.

Several cost models were implemented in PyTok. First is the model from the ARIES cost account documentation [58] where the recommended algorithms were used throughout and costs were escalated to 2025 dollars [59]. The CAD representation of the tokamak was used to estimate the power core equipment costs, with raw material costs and fabrication factors applied to the mass of each component (see table 3).

Secondly, proprietary models developed for TE by Atkins for the UK Government sponsored Advanced Modular

Table 3. Raw material cost and fabrication factor used in cost model. Raw costs are estimates based on market spot prices and supplier engagement. Fabrication factors assume that components can be produced in a factory and assembled on site.

Material	Raw Cost dollar; kg^{-1}	Fabrication Factor(#)
Boron Carbide	50.0	4.0
Lithium Metal	10.0	1.1
SS316L(N)-IG2	1.0	4.0
SS304B	2.0	4.0
Tungsten	50.0	4.0
Tungsten Boride	50.0	4.0
Tungsten Carbide	50.0	4.0
F82H	10.0	4.0
V-4 wt.%Cr-4 wt.%Ti	200.0	4.0

Reactor programme and an early ST-E1 concept were combined to generate scaling factors and extrapolate to a wider range of power plant concepts. This model has the advantage of incorporating Atkins' experience with civil nuclear power plants and providing a more up-to-date cost year of 2021, but the disadvantage that the cost structure is not the same as the now widely accepted cost accounts in the ARIES model, which align with Generation IV nuclear power plant methods. The models used in the PyFECONS tool [60] were also examined for application but offered similar methodologies in the power core component calculations and relatively minor differences in the power island estimates. The cost data shown in later sections of this report use the Atkins model, with costs escalated to 2025 dollars [59] and the Lazard model (version 18 [61]) for Levelised Cost of Electricity (LCOE) calculations. The LCOE calculations assume 60 % debt finance at 8 % interest, 40 % equity at 12 % internal rate of return (IRR), a tax rate of 40 % and a debt repayment period of 30 years. The construction period is assumed to be 7 years.

The Overnight Capital Cost (OCC) is used throughout this manuscript and is defined as:

$$\mathrm{OCC} = (1 + R_{\mathrm{contigency}}) \times (C_{\mathrm{Direct}} + C_{\mathrm{Indirect}} + C_{\mathrm{Decom}} + C_{\mathrm{Owner's}}) \tag{67}$$

where the contingency rate, $R_{\mathrm{contigency}} = 15\,\%$. The capacity-normalised OCC is frequently used for comparison to established technologies and is defined as:

$$\mathrm{OCC}_{\mathrm{normalised}} = \frac{\mathrm{OCC}}{1000 \times P_{\mathrm{e,net}}} \tag{68}$$

with units of \$/kWe.

3. Design point evolution

The process of pre-concept development consisted of several design cycles, each involving initial design point selection with PyTok followed by higher fidelity plasma physics and engineering analysis, culminating in a design update. The insights garnered from one design cycle were fed back into PyTok either as changes to parameters, or in some cases new models that better described the higher-fidelity data. Using this method ensured that the foundation of the next iteration was more solid than the previous. There are a set of high-level principles and assumptions that were kept constant throughout the process because they are based on prior knowledge of technical, commercial and supply-chain constraints. These are detailed below to give context to the design process.

3.1. Design principles, assumptions and constraints

The challenges associated with the design of a low-aspect ratio tokamak power plant, and TEs approach to solving them are described in [62]. They are briefly reiterated here as they set high-level constraints on the parameter space that was explored with PyTok during the power plant scoping studies.

3.1.1. Plasma operating principles. The key design principles applied to the design of the plasma in ST-E1 are as follows:

- **Fully non-inductive flat-top operation with EC current drive:** To realise the benefits of steady-state operation the plasma current at the flat-top plasma operating point(s) must be driven fully non-inductively. Due to the low end-to-end efficiencies of external current drive, this implies operation with a high bootstrap current fraction.
- **Solenoid to assist with ramp-up to the flat-top operating point:** While steady-state operating regimes do not require inductive current drive during flat-top, the inclusion of a central solenoid has several benefits. First, it alleviates risk associated with extrapolating solenoid-free research results to a high current, high performance power plant regime for the first time. Secondly, it reduces the time taken to ramp-up to the flat-top operating point (as demonstrated in [34]), thereby reducing the time the plant is importing electrical power from the grid, or the capacity of energy storage systems. Thirdly, during the commissioning and pilot plant operational phases it may be beneficial to have the ability to drive inductive current during the flat-top. Finally, it allows for fast control of the plasma current during flat-top in the event of any deviations from the target operating point.
- **Bootstrap current:** The nominal bootstrap current fraction should not exceed 95% to enable plasma control by actuation of EC power injection

- **LH power threshold:** The power conducted across the separatrix should be $\gtrsim 1.5$ times the LH transition power
- **Divertor power loading**: The normalised exhaust power metric should be in the range $P_{\mathrm{SOL}}/R_{\mathrm{geo}} = 20 - 30\,\mathrm{MWm}^{-1}$
- **Enhanced confinement:** It is assumed that low-aspect ratio tokamaks with $1.9 < A < 2.4$ will have enhanced confinement over larger aspect ratios $A \geqslant 2.5$, such that the ITER98(y,2) energy confinement time scaling can be used with a H-factor $\lesssim 1.4$.

3.1.2. Engineering principles. The key design principles applied to the engineering design of ST-E1 are as follows:

- **No inboard tritium breeding:** Tritium breeding materials are relatively poor fast neutron attenuators and shielding is a critical challenge in low aspect ratio tokamaks, therefore the centre column blanket should not have a tritium breeding function
- **Pure natural lithium as tritium breeder:** There are no large-scale lithium enrichment plants in operation or under construction that could supply 10 s of tonnes of fusion grade enriched lithium in the 2030 s, therefore enriched breeding materials should not be considered for ST-E1. Prior internal studies by TE indicated that pure natural lithium is the only material that could achieve TBR $\geqslant 1.15$ for $1.9 < A < 2.3$ without inboard breeding and lithium enrichment. Vanadium alloy, V-4Cr-4Ti, was selected as the breeder blanket structural material to maximise compatibility with liquid lithium and thermal power conversion efficiency; for further details of the tritium breeding blanket please refer to [63].
- **Helium as the centre column shield coolant:** Although water is an efficient coolant and has the added benefit of contributing to shielding due to its neutron moderating properties, its high chemical reactivity with metallic lithium makes it an incompatible choice with the selected breeding medium. Helium is inert, does not become radioactive from neutron interactions, and can be used at elevated temperatures, therefore it is the primary choice of coolant in the power core. It is acknowledged that, due to its transparency to neutrons, the choice of helium increases the thickness of the centre column shielding required to achieve the same magnet lifetime, thereby increasing the overall device dimensions.
- **Monolithic ReBCO HTS toroidal-field coils:** HTS toroidal field coils provide an attractive route to economic fusion power due to higher current density and higher operating temperature than LTS. TEs expertise in HTS magnet design and manufacture indicated that remountable HTS TF coils would introduce significant project risk, especially if low-resistance joints need to be made and remade in a high-radiation environment using remote handling equipment. Therefore the ST-E1 design should only consider monolithic HTS TF coils.
- **Lifetime toroidal field coils:** Replacing monolithic HTS TF coils would require the entire cold mass to be warmed up and almost complete disassembly of the tokamak with remote handling systems, which is considered incompatible with commercial availability targets ($> 80\,\%$). The TF magnets should be lifetime components.

3.2. Design space exploration

PyTok was used to explore the design space to identify configurations that satisfy the high-level requirements of the project within the constraints imposed by the plasma and engineering principles. Initially the mission of ST-E1 was technology development and de-risking, broadly aligned to the National Academies of Sciences, Engineering and Medicine's vision of a fusion pilot plant [64]. This mission required a full power life (FPL) $\geqslant 5$ years to allow testing of plasma-facing components over several environmental cycles, and the capability to demonstrate a net electric power output of $\geqslant 50$ MWe. The latter requirement was interpreted as a lower limit, therefore a target of $\geqslant 100$ MWe was set to account for uncertainties involved in low-fidelity modelling. For the pilot mission, staying within 1st stability limits was included in the plasma operating principles to minimise the cost and design risk associated with stabilising features. Figure 7 shows the high-level parameter space for these requirements with fixed $\Phi_{\mathrm{OH}} = 30$ Vs, fusion power 1000 MW and radiation corrected $H_{\mathrm{ITER98(y,2)}} = 1.4$. To generate the data, PyTok used the optimisation routine described in section 2.7 with targets, $C(\beta) = 0.9$, $f_{GW} = 0.9$, and $P_{\mathrm{SOL}}/R_{\mathrm{geo}} = 25\,\mathrm{MW\ m^{-}1}$. By following the contour of FPL $= 5$ years to the intersection with $C(\beta) = 0.9$ it can be observed that the minimum viable major radius is $\sim$4.3 m (for $B_{\mathrm{T}} = 4$ T) and the total Overnight Capital Cost (OCC) is in the region of \$8B (2025 USD).

A pilot plant at an \$8B OCC, 50 MWe output and 5-year lifetime is an unattractive investment for private sector finance, therefore the ST-E1 mission was adapted to target a $\mathrm{OCC}_{\mathrm{normalised}}$ of \$12 000 per kWe (2025 USD) and a full-power life $\geqslant 30$ years. The concept of operations was adapted to include an initial, pilot phase followed by an upgrade programme to introduce advanced power core technologies that would reduce recirculating power and enhance plasma controllability. The second phase of plasma operations would then demonstrate commercial power production and availability.

The principal means of reducing recirculating power, within the scope of the overall design philosophy, is to reduce the mass flow and associated pressure drops in the helium primary coolant system. In the pilot configuration the blanket (including first walls) and divertor are cooled by high-pressure helium, with recuperators to minimise heat rejection. The high flow rates required to cool plasma-facing surfaces means that recuperators must be large, leading to significant pressure drops and total compressor power of $\sim$200 MWe [65]. Due to the relatively low toroidal field in the region occupied by the outboard blanket, a self-cooled configuration may be feasible in the commercial phase [65], and this is assumed in the input parameters. Another enhancement assumed for the commercial phase is the ability to operate further above

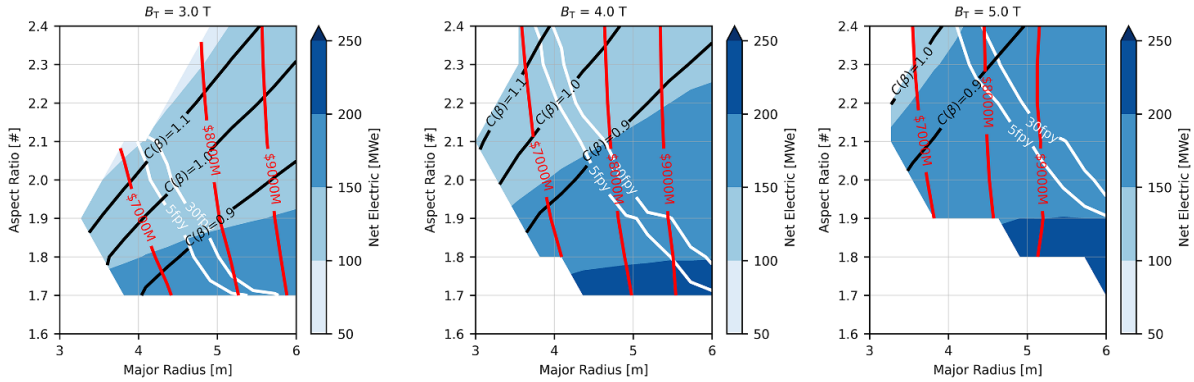

Figure 7. Net electrical output for range of major radius, aspect ratio and toroidal field strength for 30 Vs central solenoid and 1000 MW fusion power. The red lines show contours of overnight capital cost in 2025 dollars.

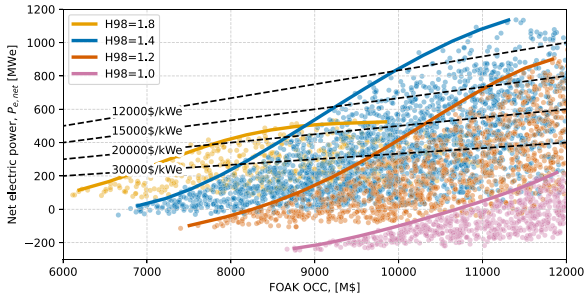

Figure 8. PyTok scan data with varying major radius, aspect ratio, toroidal field and fusion power, for a range of energy confinement enhancement factors, to indicate the net electric output needed to meet the requirement for normalised overnight capital cost of $12 000/kWe for a First-of-a-Kind (FOAK) commercial power plant.

the no-wall β limit using passive and active stabilisation features.

Based on the updated assumptions, a broad parameter scan was performed to determine the net electric power output needed to meet the $\mathrm{OCC_{normalised}}$ requirement in the commercial phase. The data, shown in figure 8, was generated by performing a large ensemble parameter space scan using PyTok, varying major radius, aspect ratio, toroidal field, fusion power and energy-confinement time enhancement factor. For the scan the stability targets were updated to $C(\beta) = 1.0$ and $f_{GW} = 1.0$, but the power-handling metric was retained at $P_{\mathrm{SOL}}/R_{\mathrm{geo}} = 25\,\mathrm{MW\ m^{-}1}$. The optimiser is not always successful because an operating point that satisfies all the target parameters may not exist. These points can be filtered from the final dataset and allows the impact of these stability limits to be determined. The ensemble scan uses the quasi-random Sobol sampling method to scan over the device geometry, magnetic field, and target fusion power. These scans were performed for different values of the radiation corrected energy confinement enhancement factor (H-factor) relative to the ITER98(y,2) scaling, H98*. All other assumptions and inputs were held constant across the scan. The full dataset is plotted along with a trend line representing the design points with the lowest OCC for a given $P_{\mathrm{e,net}}$.

Figure 8 shows that for $H_{\mathrm{ITER98(y,2)}} = 1.4$ and $P_{\mathrm{e,net}} > 800$ MWe the requirement is met with the lowest OCC of ∼$10B (2025 USD). The plot illustrates several other key points. First, there is a strong economy of scale, indicated by the fact that as the OCC (which is analogous to the device scale) increases, the minimum cost per unit installed capacity ($/kWe) reduces. Secondly, the plant performance is strongly dependent on the assumed plasma energy confinement enhancement factor. Steady-state operating points are highly coupled due to the need for high bootstrap current fractions, and as a result, performance is more strongly dependent on confinement than in inductively driven plasmas. Thirdly, the highest energy confinement does not always correspond to the lowest installed capacity cost, as shown by the trend of the $H_{\mathrm{ITER98(y,2)}} = 1.8$ curve. This may at first seem counter intuitive, but can be explained by the fact that H-factor determines the amount of fusion power required to reach a certain fusion gain, with higher H-factors requiring lower fusion powers. As H-factor increases, there comes a point where the plasma ignites (or reaches the maximum allowable fusion gain) and it is not possible to increase fusion power further, without degrading confinement.

Figure 9 reinforces the mission choice by demonstrating how the anticipated LCOE varies with installed capacity. The data indicates that there is a broad design space for a plant producing on the order of 1 GWe net output that could compete with US Nuclear and new-build coal plants (LCOE data from Lazard [61]).

It was estimated that $\simeq 2500\,\mathrm{MW}$ fusion power would be required to generate $P_{\mathrm{e,net}} > 800\,\mathrm{MWe}$, therefore the parameter space shown in figure 7 was rescanned with the commercial-phase assumptions and higher target fusion power. When these considerations are built into the PyTok model the previous parameter landscape changes to that shown in figure 10.

The plots show that the requirements of the commercial plant (namely, $\mathrm{OCC_{normalised}} \leqslant \$12\,000\,/\mathrm{kWe}$ and full-power life $\geqslant 30$ years) can be fulfilled for designs with a major radius of $\gtrsim 4.9$ m while also operating only marginally above the no-wall β limit, $C(\beta) \leqslant 1.1$. A major radius of 5.0 m was therefore selected to constrain the solution space and satisfy

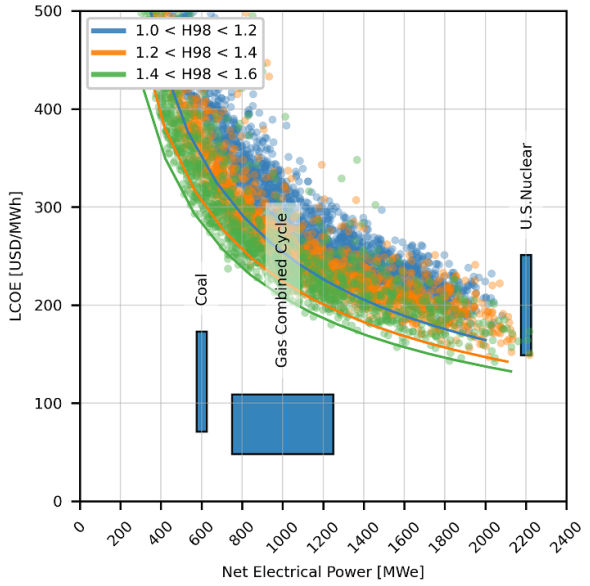

Figure 9. PyTok scan data with varying major radius, aspect ratio, toroidal field, fusion power and $H_{\mathrm{ITER98(y,2)}}$ demonstrating that commercial competitiveness improves with scale. A net electric output of 1 GWe would make ST-E1 cost competitive with US Nuclear and new-build coal plants (LCOE data from Lazard [61]).

the mission, while keeping the device size and OCC as low as practicable.

Figure 11(*b*) slices the power plant dataset at 5.0 m to show the parameter surface for aspect ratio and toroidal field. There are a range of points along the $C(\beta) = 1.1$ and 30 FPY contours with varying aspect ratio and toroidal magnetic field strength that show similar performance. A selection of these points at different aspect ratios are summarised in table 4. The 'Height' column is used as a proxy for the compactness of the tokamak; the radial extent of the device has a relatively weak dependence on aspect ratio because the toroidal field coil size is driven by the maintenance scheme, whereas the height of the device varies more strongly with aspect ratio through a combination of the minor radius and stable elongation, both of which are inversely proportional to aspect ratio. Analysis of a refined breeder blanket concept indicated that the TBR would be reduced by several percent once additional features and structural divisions were incorporated, therefore aspect ratio 2.3 is the maximum considered for security of tritium fuel supply. This table highlights one of the key design space tradeoffs, the choice between lower aspect ratio or increased magnetic field, which results from the constraints on the inboard radial build. Further assessment using higher fidelity models is required to determine if there is an optimum within the identified range. One factor of particular importance is the dependence of plasma confinement on aspect ratio and magnetic field.

For a pre-concept design, an optimum design point is not needed to substantiate requirements, therefore a reference configuration was selected based on engineering judgement that favoured low elongation and plasma current, i.e. higher field and aspect ratio. It was decided that for major radius 5.0 m the aspect ratio should be 2.3, constraining the toroidal field to a maximum value of 5.25 T. Table 4 indicates that this is the most expensive of the configurations in the parameter space, but a difference of $\sim$5 % between the lowest and highest values was not considered significant in the context of cost model uncertainties.

Optimisation of other inputs for the chosen high-level parameters was conducted, which resulted in an increase in f_{BS} and predicted $P_{\mathrm{e,net}}$. The PyTok parameters for the pilot and commercial phases are shown in table 5. The pilot data provided the reference design point (RDP) for higher-fidelity analyses focussing on the plasma flat-top scenario [66]; ramp-up [34]; power exhaust [67]; heating and current drive [30]; integrated plasma-magnet modelling [41]; power core maintenance [44]; blanket and fuel-cycle engineering [63]; radiation effects and shielding [68]; and thermal power processing and electrical power generation [65]. It is expected that these detailed analyses will provide feedback that will evolve and refine the RDP for the next stage of the ST-E1 concept design.

3.3. Uncertainty

In pre-concept design the ability to articulate the uncertainty and risk of design decisions helps to guide technology road maps, programme management and stakeholder expectations. PyTok includes a module that enables specified input parameters to be sampled from probability distributions, applying the Monte Carlo method to the underlying deterministic PyTok framework. Key uncertainties of the commercial design point were explored while keeping the high-level design parameters fixed. The variables were: temperature and density profiles; normalised current drive efficiency; maximum f_{GW}; bootstrap fraction modifier; miscellaneous plant load and the tritium plant load. The value of $H_{\mathrm{ITER98(y,2)}}$ was sampled from a triangular distribution, with minimum value 1.0, most likely 1.4 and maximum 1.5. For each case the PyTok optimiser adjusted the plasma operating parameters to ensure that the fusion power target of 2400 MW was met, but to achieve this the injected EC power was allowed to vary, thus the net electric power and the capital cost was expected to vary. The analysis was thus designed to indicate how the plant configuration and cost could vary as increasingly mature plasma-physics understanding alters the range of possible operating scenarios.

The net electric output for 10 000 samples is shown in figure 12. The distribution shows that the probability of achieving the mission objective for the commercial phase of $>$ 800 MWe is 92%. To achieve similar net electric output while varying plasma parameters requires that the ECCD power changes, which has a significant effect on the capital cost. Figure 13 shows that, given the net electric distribution, the probability of achieving the target of $\mathrm{OCC_{normalised}} < \$12\,000$ kWe is 26%, and the median cost is \$12 800 kWe. The risk can be mitigated by reducing the unit cost of installed EC current drive capacity or increasing unit efficiency, such that the capital cost is less sensitive to variations in the predicted demand.

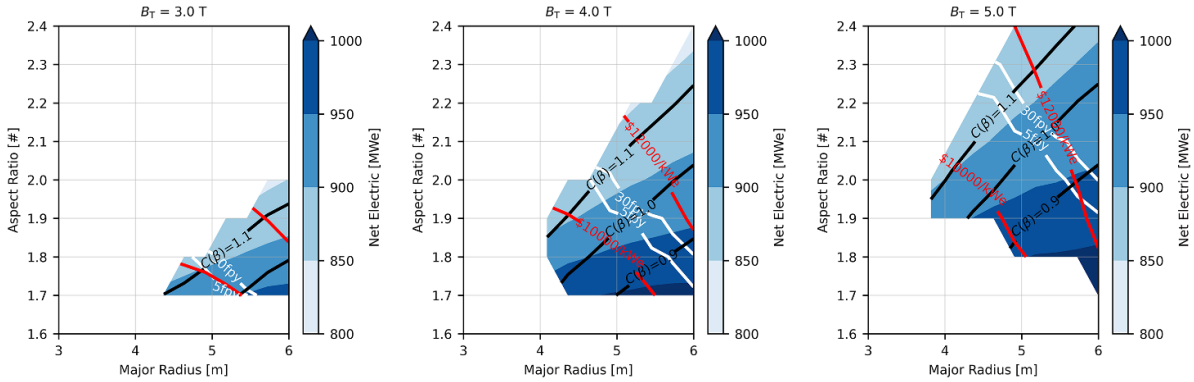

Figure 10. Net electrical output for range of major radius, aspect ratio and toroidal field strength for 30 Vs central solenoid and 2500 MW fusion power. Red lines are the normalised capital cost in 2025 dollars.

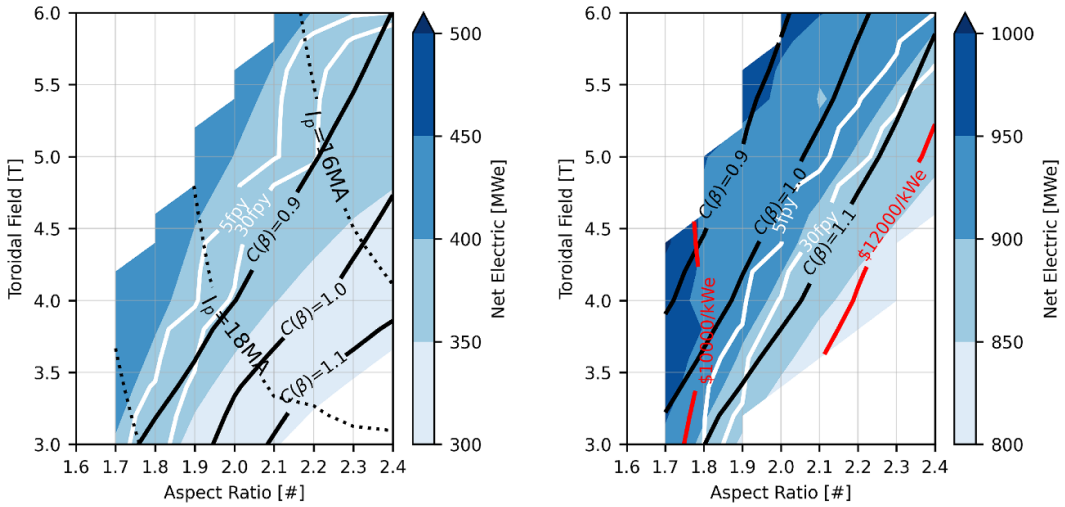

Figure 11. Design space at major radius of 5 m for pilot phase (left) and commercial phase (right) of operations.

Table 4. Range of commercial design points with equivalent performance based on PyTok analysis. The tritium breeding ratio (TBR) is based on a simplified geometry and represents an estimate of the maximum achievable. The normalised overnight capital cost (OCC_n) is in 2025 USD.

A	B_T	I_p	TBR	Height	OCC_n
—	T	MA	—	m	$/kWe
1.90	3.25	22.2	1.28	19.6	11 200
2.00	4.00	21.0	1.26	18.7	11 300
2.10	4.40	20.1	1.25	17.8	11 500
2.20	4.90	19.3	1.23	17.3	11 700
2.30	5.25	18.7	1.21	16.5	11 800

4. Commercial outlook

A first-of-a-kind commercial plant featuring novel technologies suffers from high costs due to the immature supply chain and lack of delivery experience. For a longer-term commercial outlook and comparison with mature power plant technologies a 10th-of-a-kind (TOAK) plant was considered, in which learning rates were applied to major cost accounts to reflect the increase in efficiency in the supply chain and project delivery. The rates for each account and the projected relative cost for $1 < N < 10$ are shown in figure 14.

Due to the high up-front capital cost of the ST-E1 generation of plants, commercial success will depend on the capacity factor. Fusion plants should aim to equal or exceed nuclear fission, which had global average capacity factor across all reactor types and ages of 83% in 2025 [69]. The ST-E1 design focuses on both duty cycle and availability of the power core; these factors motivate the focus on steady-state plasma operations and on the power core maintenance scheme, which does not require a break of the magnet cryostat vacuum and is in principle parallelisable [44]. An estimate of the duration of a major maintenance outage was beyond the scope

Table 5. yTok design points for ST-E1. The Pilot configuration was adopted as the Reference Design Point (RDP) for higher-fidelity analysis used to substantiate the requirements of the pre-concept design. The Commercial configuration is an evolution of the RDP that indicates how ST-E1 could fulfil its commercial mission. The parameter C_{β_N} is the ratio of β_N to the no-wall limit, and C_{β_p} is the ratio of β_p to the no-wall limit.

Parameter	Unit	Pilot	Commercial
R_{geo} [m]	m	5.0	
B_T [T]	T	5.25	
A [-]	—	2.3	
κ/δ	—	2.42/0.5	
$\langle n_e \rangle$	m^{-3}	1.16×10^{20}	1.31×10^{20}
$\langle T_e \rangle$	keV	5.9	7.3
Z_{eff}	—	2.19	2.76
I_p	MA	14.8	15.4
f_{bs}	%	88	88
P_{fus}	MW	1573	2400
P_{ECCD}	MW	73	66
Q_{fus}	—	21.5	36.5
$P_{rad,core}/P_{core}$	%	68	77
P_{SOL}	MW	125	125
$P_{LH,nom}$	MW	83	80
P_{NWL}	MW m^{-2}	1.6	2.4
P_{RWL}	MW m^{-2}	0.45	0.65
P_{SOL}/R_{geo}	MW m^{-1}	25	25
$H_{ITER98(y,2)}$	—	1.4	1.4
β_N	—	3.38	3.85
C_{β_N}	—	0.85	1.0
C_{β_p}	—	1.0	1.15
f_{GW}^{ped}	—	1.0	1.0
TBR	—	—	1.15
$P_{t,gross}$	MWt	1755	2770
$P_{e,gross}$	MWe	824	1300
$P_{e,pumping}$	MWe	161	100
$P_{e,H\&CD}$	MWe	145	142
$P_{e,cryo}$	MWe	9	9
$P_{e,plant}$	MWe	30	30
$P_{e,net}$	MWe	478	1020
Q_{eng}	—	2.4	4.6
OCC	$B	10.8	11.9

of pre-concept design but an upper bound of 6 months was used within PyTok modelling to estimate the capacity factor for LCOE calculations. With the 6 month value and an operational period of 4.2 years (based on neutron wall loading of 2.4 MW m^{-2} giving an estimated 24 dpa per year in steel, and a 100 dpa lifetime) a capacity factor of 90% is theoretically achievable. While this is unlikely to be realised on ST-E1, it is assumed that it will be demonstrated on a TOAK based on the same design. Using these input assumptions the ST-E1 TOAK would have $OCC_{normalised}$ of 8700kWe and an LCOE of $160/MWh (2025 USD) using the Lazard methodology [61]. This value is at the lower end of the range of $140-$550/MWh (2021 USD) identified by Araiinejad and Shrivan for a NOAK fusion power plant based on a modified ARC concept [70]. When inflated to base year 2025 the minimum value in the range is $165 MWh, therefore the NOAK estimate is at the minimum. There are significant differences in methodologies between the cost estimates so the comparison is not intended to be definitive, but to add credibility to the conclusion.

A base-load generating station with LCOE of $160 MWh would be competitive with other power-generating technologies, including renewables when firming costs are taken into account [70]. However, figure 9 indicates that the six-tenths rule of thermal power generation costs apply to the fusion power plant concept, therefore increasing the capacity may be advantageous. Figure 15 shows the trend for a TOAK plant with the same underlying design principles utilised for the ST-E1 study and indicates that LCOE $<$ $100MWh may be achievable if the output of a single unit is $\geqslant$ 1600 MWe, similar to the capacity of the European Pressurised Water Reactor (EPR) under construction at Hinckley Point C and Sizewell C in the U.K.

Regulated electric utilities in the U.S. typically evaluate new generation investments through a simple but rigorous lens: the ability to deliver safe, reliable, and lowest-reasonable-cost power to customers over decades. In this context, $OCC_{normalised}$ becomes a primary decision metric, because it directly drives the rate base, customer tariffs,

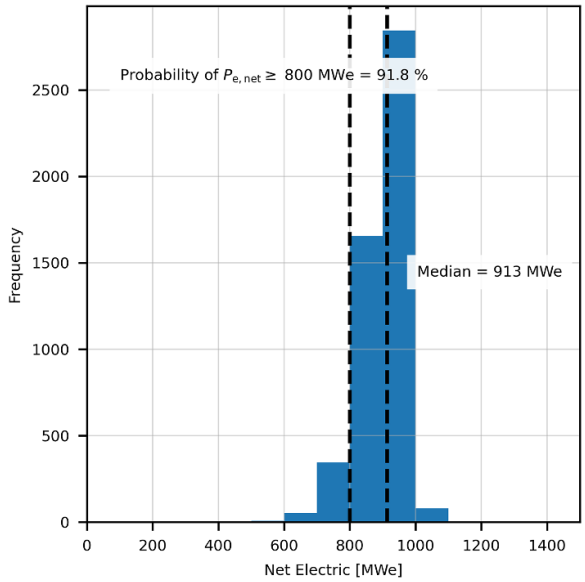

Figure 12. Distribution of net electric output for the commercial plant configuration obtained by Monte Carlo analysis varying density and temperature profile parameters, normalised current drive efficiency, bootstrap fraction, maximum Greenwald fraction and $H_{\mathrm{ITER98(y,2)}}$.

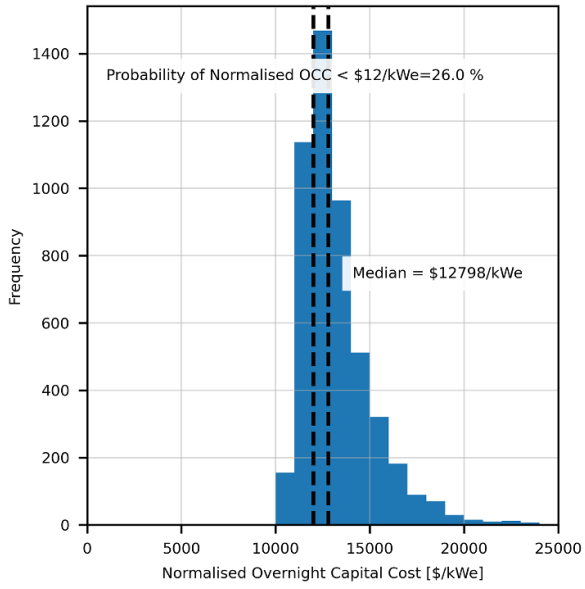

Figure 13. Distribution of normalised overnight capital cost for the commercial phase obtained by Monte Carlo analysis varying density and temperature profile parameters, normalised current drive efficiency, bootstrap fraction, maximum Greenwald fraction and $H_{\mathrm{ITER98(y,2)}}$.

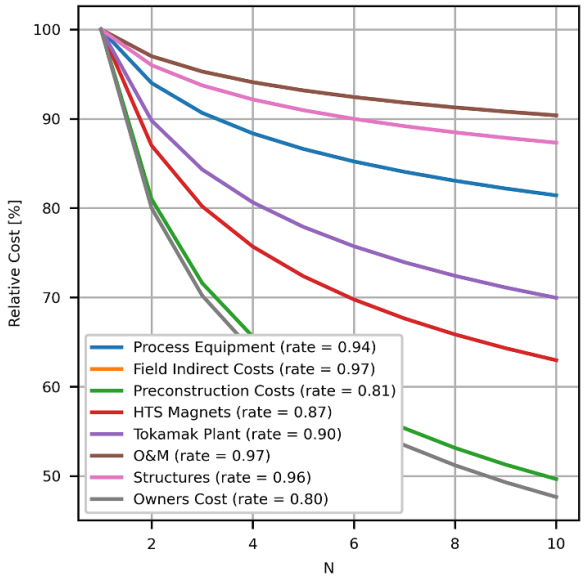

Figure 14. Learning rates for major cost areas used to project from First-of-a-Kind to Tenth-of-a-Kind fusion power plant with the same underlying design.

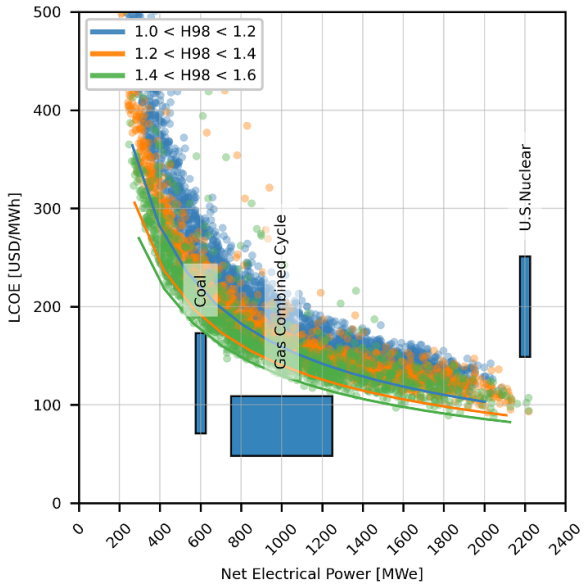

Figure 15. PyTok scan data with varying major radius, aspect ratio, toroidal field, fusion power and $H_{\mathrm{ITER98(y,2)}}$ for a 10th-of-a-kind plant, indicating that levelised cost of electricity $<$ \$100MWh could be achieved for 1600 MWe capacity. The data also shows that there is a broad range of design points that would be competitive with US Nuclear and new-build coal plants [61].

and the likelihood of regulatory approval. Technologies with predictable construction schedules, standardised designs, and well-understood operating costs are strongly favoured, as they reduce financing risk and protect customers from cost overruns. Once fusion demonstrates a credible path to $\mathrm{OCC_{normalised}}$ and LCOE that is competitive with other firm, low-emission generation—and shows that projects can be financed on conventional utility balance sheets with regulatory cost recovery—it becomes naturally aligned with the regulated utility model. At that point, fusion will be a financeable infrastructure asset, opening the door to broad deployment by utilities seeking clean, long-lived, reliable, and affordable power. TE received feedback from several U.S. utilities that confirmed the availability of this financing model when fusion reaches sufficient technological maturity. Furthermore, given its preferable environmental profile,

thus reduced regulatory requirements compared to fission and other conventional technologies, fusion would be highly attractive to such utilities and independent power producers once it reaches commercial parity. The ST-E1 concept provides a capital efficient route to commercial viability by de-risking technologies at full scale in the pilot phase of the project.

5. Concluding remarks

Fusion power plants with pulsed power cores may be severely constrained by cyclic fatigue, leading to frequent maintenance intervals. In the case of a compact inductively-driven reactor the machine will be pulsed ∼500000 times over a 20 year lifetime, assuming a 1000 second pulse length, and the plasma-facing components will suffer thermal fatigue from extreme cyclic surface heat loading. TE proposes an alternative approach focussed on a low aspect ratio tokamak with fully non-inductive auxiliary current drive, enabling efficient, steady-state plasmas. A pre-concept design of this fusion power plant, ST-E1, has been completed in 18 months, with an integrated team of physicists and engineers, supported by new tools and efficient workflows. The internally-developed systems code PyTok was instrumental in producing self-consistent design points to aid substantiation of the high-level project requirements, providing a common basis for higher-fidelity analysis and an upgradeable tool that enabled the iterative improvement of technical system integration.

It was found that configurations for a pilot plant are too expensive to be attractive to private capital, therefore a staged approach was adopted. The permanent features of a commercially-viable power plant are specified, but the initial configuration of the tokamak is designed to fulfil a pilot plant mission of addressing outstanding science and technology gaps while demonstrating significant power output to the grid. The tokamak power core is designed to be upgraded, and on completion of the pilot phase components will be replaced to enable greater power production, providing the blueprint for a fleet of commercial fusion power plants.

At the pre-concept level of maturity, it has been shown that the requirements of a commercially-competitive fusion power plant can be realised by a tokamak power core with a major radius of 5.0 m, aspect ratio $1.9 < A < 2.3$ and toroidal field $3.25 < B_{\mathrm{T}} < 5.25$ T. Further work is needed to determine the optimum design point, but the pre-concept investigations provide the foundation for the next stage in concept development, and chart a path to commercial fusion energy.

Acknowledgments

This work was undertaken as part of the US Department of Energy Milestone-based Fusion Development Program.

Funding

Tokamak Energy acknowledges U.S. Federal support for this work under TIA DE-SC0024889.

ORCID iDs

C.L. Wilson 0009-0007-8860-3867
M.J. Ginsberg 0000-0003-0423-7032
N. Hinton 0009-0006-4693-4054
E.N.J. Maartensson 0009-0000-7289-8516
S.A.M. McNamara 0000-0002-0477-5247
E. Yildirim 0000-0002-1903-1857

References

[1] Swanson C. 2022 A survey of fusion reactor systems codes, and how you can help (available at: https://storage.googleapis.com/pppl-theory-web-content/news/seminars/20220609-Swanson.pdf) (Accessed 14 October 2025)
[2] Costley A.E., Hugill J. and Buxton P.F. 2015 On the power and size of tokamak fusion pilot plants and reactors *Nucl. Fusion* **55** 033001
[3] McNamara S.A.M. *et al* 2024 Overview of recent results from the ST40 compact high-field spherical tokamak *Nucl. Fusion* **64** 112020
[4] Kovari M., Kemp R., Lux H., Knight P., Morris J. and Ward D.J. 2014 PROCESS: a systems code for fusion power plants-Part 1: Physics *Fusion Eng. Des.* **89** 3054–69
[5] Kovari M., Fox F., Harrington C., Kembleton R., Knight P., Lux H. and Morris J. 2016 PROCESS: a systems code for fusion power plants—Part 2: engineering *Fusion Eng. Des.* **104** 9–20
[6] Reux C. *et al* (ITM-TF Contributors) 2015 DEMO reactor design using the new modular system code SYCOMORE *Nucl. Fusion* **55** 073011
[7] Coleman M. and McIntosh S. 2019 Blueprint: a novel approach to fusion reactor design *Fusion Eng. Des.* **139** 26–38
[8] Freecad (available at: www.freecad.org/)
[9] Hunter J.D. 2007 Matplotlib: a 2D graphics environment *Comput. Sci. Eng.* **9** 90–95
[10] Plotly Technologies Inc. 2015 Collaborative data science (available at: https://plot.ly)
[11] Badalassi V., Sircar A., Solberg J.M., Bae J.W., Borowiec K., Huang P., Smolentsev S. and Peterson E. 2023 Fermi: Fusion energy reactor models integrator *Fusion Sci. Technol.* **79** 345–79
[12] Collins C.S. *et al* 2024 Development of an integrated modeling framework for fusion reactor design and assessment *Technical Report ORNL/TOM-2024/3520* Oak Ridge National Laboratory
[13] Bachmann S. *et al* 2024 Re-design of EU DEMO with a low aspect ratio *Fusion Eng. Des.* **204** 114518
[14] Sarasola X., Bruzzone P., Sedlak K., Corato V., Giannini L., Bachmann C., Luongo C. and Siccinio M. 2023 Parametric studies of the EU DEMO central solenoid *IEEE Trans. Appl. Supercond.* **33** 1–5
[15] McKinney W. 2010 Data structures for statistical computing in python *Proc. 9th Python in Science Conf.* (*Austin, Texas*, *28 June–3 July 2010*) ed S. van der Walt and J. Millman pp 56–61
[16] The pandas development team 2024 pandas-dev/pandas: Pandas (available at: https://doi.org/10.5281/zenodo.13819579)
[17] Snyder P.B., Groebner R.J., Leonard A.W., Osborne T.H. and Wilson H.R. 2009 Development and validation of a predictive model for the pedestal height *Phys. Plasmas* **16** 056118
[18] Miller R.L., Chu M.S., Greene J.M., Lin-Liu Y.R. and Waltz R.E. 1998 Noncircular, finite aspect ratio, local equilibrium model, phys *Plasmas* **5** 973–8

[19] Ludwig G.O., Andrade M.C.R., Gryaznevich M. and Todd T.N. 2009 Physics performance analysis of low-power tokamak reactors *Nucl. Fusion* **49** 085026

[20] Estrada-Mila C., Candy J. and Waltz R.E. 2006 Turbulent transport of alpha particles in reactor plasmas *Phys. Plasmas* **13** 112303

[21] Beresnyak A. 2023 *NRL Plasma Formulary* (Naval Research Laboratory)

[22] Bosch H.-S. and Hale G.M. 1992 Improved formulas for fusion cross-sections and thermal reactivities *Nucl. Fusion* **32** 611

[23] Vernickel H. and Bohdansky J. 1978 A general formula for impurity radiation loss of fusion plasmas in corona equilibrium *Nucl. Fusion* **18** 1467

[24] Lux H., Kemp R., Ward D.J. and Sertoli M. 2015 Impurity radiation in demo systems modelling *Fusion Eng. Des.* **101** 42–51

[25] Petty C.C. 2008 Sizing up plasmas using dimensionless parameters *Phys. Plasmas* **15** 080501

[26] Kurskiev G.S. *et al* 2021 Energy confinement in the spherical tokamak globus-m2 with a toroidal magnetic field reaching 0.8 t *Nucl. Fusion* **62** 016011

[27] Buxton P.F., Connor J.W., Costley A.E., Gryaznevich M.P. and McNamara S. 2019 On the energy confinement time in spherical tokamaks: implications for the design of pilot plants and fusion reactors *Plasma Phys. Control. Fusion* **61** 035006

[28] Takizuka T. 2004 Roles of aspect ratio, absolute *B* and effective *Z* of the H-mode power threshold in tokamaks of the ITPA database *Plasma Phys. Control. Fusion* **46** A227

[29] Andrade M.C.R. and Ludwig G.O. 2008 Scaling of bootstrap current on equilibrium and plasma profile parameters in tokamak plasmas *Plasma Phys. Control. Fusion* **50** 065001

[30] Lopez N., McAdam A., Stirling J., Takase Y., Alieva A., Zhang X., Borscz M., McNamara S. and Maartensson E.N.J. 2026 Auxiliary heating and current-drive physics for the ST-E1 fusion power plant *Nucl. Fusion* **66** 086010

[31] Uckan N.A. *et al* 1990 ITER physics design guidelines: 1989 *Technical Report* International Atomic Energy Agency

[32] Mitarai O., Yoshino R. and Ushigusa K. 2002 Plasma current ramp-up assisted by outer vertical field coils in a high aspect ratio tokamak *Nucl. Fusion* **42** 1257

[33] Menard J.E. *et al* (NSTX Research Team) 2001 Ohmic flux consumption during initial operation of the NSTX spherical torus *Nucl. Fusion* **41** 1197

[34] Zhang L., Borscz M., Kang J., Lopez N., Maartensson E.N.J., McNamara S., Scarpari M., Marsden C. and Takase Y. 2026 Time-dependent scenario modelling for the ST-E1 fusion power plant *Nucl. Fusion* **66** 086009

[35] Menard J.E., Bell M.G., Bell R.E., Gates D.A., Kaye S.M., LeBlanc B.P., Maingi R., Sabbagh S.A., Soukhanovskii V. and Stutman D. 2004 Aspect ratio scaling of ideal no-wall stability limits in high bootstrap fraction tokamak plasmas *Phys. Plasmas* **11** 639–46

[36] Medvedev S., Abouelazayem S., Dnestrovskii A., Gryaznevich M., Janky F., McNamara S.A.M. and Romanelli M. (the Tokamak Energy FPP Team) 2025 *Beta Limits, Pedestals and Controllability in fpp. 2025 Sherwood Fusion Theory Conf.* (*New York, NY, USA*, *7–9 April 2025*)

[37] Stambaugh R.D. *et al* 2011 Fusion nuclear science facility candidates *Fusion Sci. Technol.* **59** 279–307

[38] Thomas Eich A.W.L. *et al* 2013 Scaling of the tokamak near the scrape-off layer H-mode power width and implications for ITER *Nucl. Fusion* **53** 093031

[39] Thornton A.J. and Kirk A. (the MAST Team) 2014 Scaling of the scrape-off layer width during inter-ELM H modes on MAST as measured by infrared thermography *Plasma Phys. Control. Fusion* **56** 055008

[40] Virtanen P. *et al* (SciPy 1.0 Contributors) 2020 SciPy 1.0: fundamental algorithms for scientific computing in python *Nat. Methods* **17** 261–72

[41] Maartensson E.N.J. *et al* (ST-E1 Team) 2026 Integrated physics and magnet design for the ST-E1 fusion power plant *Nucl. Fusion* **66** 086007

[42] Project rat (available at: https://rat-gui.com/library.html) (Accessed 3 November 2025)

[43] Morris J., Kemp R., Kovari M., Last J. and Knight P. 2015 Implications of toroidal field coil stress limits on power plant design using process *Fusion Eng. Des.* **98-99** 1118–21

[44] Willis J., Scott A., Pocock R., Thwaites R., Godhani V., Chandrasekhar K., Cheema P., England J., Shone A. and Danisworo O. 2026 Maintenance strategy, structural design and site layout of the ST-E1 fusion power plant *Nucl. Fusion* **66** 086006

[45] Hong B.G., Hwang Y.S., Kang J.S., Lee D.W., Joo H.G. and Ono M. 2011 Conceptual design study of a superconducting spherical tokamak reactor with a self-consistent system analysis code *Nucl. Fusion* **51** 113013

[46] Engle W.W. 1967 A users manual for anisn: a one dimensional discrete ordinates transport code with anisotropic scattering *Technical Report* Oak Ridge Gaseous Diffusion Plant, Tenn (available at: www.osti.gov/biblio/4448708)

[47] Fischer D.X., Prokopec R. and Eisterer M. 2018 The effect of fast neutron irradiation on the superconducting properties of rebco coated conductors with and without artificial pinning centers *Supercond. Sci. Technol.* **31** 044006

[48] Portyanikhin V. 2025 PyFluids: simple, full-featured, lightweight coolprop wrapper for python Version 2.9.0. Python package available on PyPI (available at: https://github.com/portyanikhin/PyFluids)

[49] Ahrens J., Geveci B. and Law C. 2005 Paraview: an end-user tool for large data visualization *The Visualization Handbook* (Academic) pp 717–31 (available at: https://doi.org/10.1016/B978-012387582-2/50038-1)

[50] Paramak. (available at: https://fusion-energy.github.io/paramak/stable/index.html)

[51] Allison J. *et al* 2016 Recent developments in geant4 *Nucl. Instrum. Methods Phys. Res. A* **835** 186–225

[52] Agnostelli S. *et al* 2006 Geant4 - a simulation toolkit *Nucl. Instrum. Methods Phys. Res. A* **506** 250–303

[53] Allison J. *et al* 2006 Geant4 development and applications *IEEE Trans. Nucl. Sci.* **53** 270–8

[54] Geuzaine C. and Remacle J.-F. 2009 Gmsh: a 3-D finite element mesh generator with built-in pre- and post-processing facilities *Int. J. Numer. Methods Eng.* **79** 1309–31

[55] Davis A. and Turner A. 2011 Application of novel global variance reduction methods to fusion radiation transport problems *Int. Conf. Mathematics and Computational Methods Applied to Nuclear Science and Engineering (M&C 2011)* (*Rio de Janeiro, Brazil*, *8–12 May 2011*) p 5

[56] Chapman R. 2025 Developing integrated cost models for fusion power plants *J. Fusion Energy* **44** 43

[57] Lux H., Brown C. and Cowan J.R. 2024 Reference class forecasting and its application to fusion power plant cost estimates *IEEE Trans. Plasma Sci.* **52** 3628–33

[58] Waganer L.M. 2013 Aries cost account documentation UCSD-CER-13-01

[59] Federal reserve economic data 2025 (available at: https://fred.stlouisfed.org) (Accessed 21 May 2025)

[60] Python fusion economics (available at: https://github.com/woodruff-scientific-ltd/pyfecons)

[61] Levelized cost of energy+ 2025 (available at: www.lazard.com/news-announcements/lazard-releases-2025-levelized-cost-of-energyplus-report-pr/)
[62] Willis J. *et al* 2026 Tokamak Energy's pre-concept design for a fusion power plant: an overview of ST-E1 *Nucl. Fusion* **66** 086001
[63] Yildirim E., Mohamed M.K.E., Trueba J., Suhardjo R., Robinson M., Wilson C., Naish J. and Kumar A. 2026 Tritium production and processing systems for ST-E1 *Nucl. Fusion* **66** 086004
[64] National Academies of Sciences, Engineering, and Medicine 2021 *Bringing Fusion to the U.S. Grid* (The National Academies Press)
[65] Mohamed M.K.E. *et al* 2026 Thermal management and net-power evaluation of the ST-E1 fusion power plant *Nucl. Fusion* **66** 086005
[66] McNamara S. *et al* 2026 Physics basis for the reference flat-top plasma scenario in the ST-E1 fusion power plant *Nucl. Fusion* **66** 086008
[67] Robinson M. *et al* 2026 Power and particle exhaust in the ST-E1 fusion power plant *Nucl. Fusion* **66** 086011
[68] Chandrasekhar K., Wilson C., Levine S., Godhani V., Naish J. and Irukuvarghula S. 2026 Nuclear technology considerations and neutronics for the ST-E1 fusion power plant *Nucl. Fusion* **66** 086003
[69] World Nuclear Association 2025 World Nuclear Performance Report 2025 *Technical Report* (available at: https://world-nuclear.org/images/articles/World%20Nuclear%20Performance%20Report%202025.pdf)
[70] Araiinejad L.S. and Shirvan K. 2025 Techno-economic analysis of deuterium-tritium magnetic confinement fusion power plants *Appl. Energy* **401** 126567